

# Monitoring of CaCO 3 Nanoscale Structuration through Real-Time Liquid Phase Transmission Electron Microscopy and Hyperpolarized NMR

Vinavadini Ramnarain, Tristan Georges, Nathaly Ortiz Peña, Dris Ihiawakrim, Mariana Longuinho, Hervé Bulou, Christel Gervais, Clément Sanchez, Thierry Azaïs, Ovidiu Ersen

▶ **To cite this version:**

Vinavadini Ramnarain, Tristan Georges, Nathaly Ortiz Peña, Dris Ihiawakrim, Mariana Longuinho, et al.. Monitoring of CaCO 3 Nanoscale Structuration through Real-Time Liquid Phase Transmission Electron Microscopy and Hyperpolarized NMR. Journal of the American Chemical Society, 2022, 144 (33), pp.15236-15251. 10.1021/jacs.2c05731 . hal-03868061

**HAL Id: hal-03868061**
**https://hal.science/hal-03868061**

Submitted on 24 Nov 2022

**HAL** is a multi-disciplinary open access archive for the deposit and dissemination of scientific research documents, whether they are published or not. The documents may come from teaching and research institutions in France or abroad, or from public or private research centers.

L'archive ouverte pluridisciplinaire **HAL**, est destinée au dépôt et à la diffusion de documents scientifiques de niveau recherche, publiés ou non, émanant des établissements d'enseignement et de recherche français ou étrangers, des laboratoires publics ou privés.

# Monitoring of $CaCO_3$ nanoscale structuration through real-time liquid phase TEM and hyperpolarized NMR

*Vinavadini Ramnarain[1,6], Tristan Georges[2], Nathaly Ortiz Peña[3], Dris Ihiawakrim[1,6], Mariana Longuinho[4,5], Hervé Bulou[1,6], Christel Gervais[2], Clément Sanchez[2,7], Thierry Azaïs[2*], Ovidiu Ersen[1,6*]*

[1]Institut de Physique et Chimie des Matériaux Strasbourg, 23 Rue du Loess Strasbourg Cedex2, France

[2]Laboratoire de Chimie de Matière Condensé de Paris, Sorbonne Université, Paris, France

[3]Laboratoire Matériaux et Phénomènes Quantiques F75025 Paris Cedex 13, France

[4]CBPF, Rua Dr Xavier Sigaud, 150- Urca I CEP: 22 290-180 I Rio de Janeiro, Brasil

[5]UFRJ, Av Pedro Calmon, 550, Edificio da Reitoria, Ilha de do Fundao, Rio de Janeiro, RJ, CEP 21941-901, Brasil

[6]ICFRC, 8 allée Gaspard Monge, 67000, FRANCE

[7]USIAS, Université de Strasbourg, France

*corresponding authors

## Abstract

Calcium carbonate ($CaCO_3$) is one of the most significant biominerals in Nature. Living organisms are able to control its biomineralization by means of an organic matrix to tailor myriad of hybrid functional materials. The soluble organic components are often proteins rich in acidic amino-acids such as L-Aspartic acid. Whilst several studies have demonstrated the influence of amino acids on the crystallization of calcium carbonate, nanoscopic insight of their impact on $CaCO_3$ mineralization, in particular at the early stages, is still lacking. Herein, we implement Liquid Phase Transmission Electron Microscopy (LP-TEM) to visualize in real-time and at the nanoscale the prenucleation stages of $CaCO_3$ formation. We observe that L-Aspartic acid favors the formation of individual and aggregated pre-nucleation clusters which are found stable for several minutes before the transformation into ACC nanoparticles. Combination with hyperpolarized solid state Nuclear Magnetic Resonance (DNP NMR) and DFT calculations allow shedding light on the underlying mechanism at the prenucleation stage. The promoting nature of L-Aspartic acid with respect to pre-nucleation clusters is explained by specific interactions with both $Ca^{2+}$ and carbonates and the stabilization of the $Ca^{2+}$-$CO_3^{2-}$/$HCO_3^-$ ion pairs favoring the formation and stabilization of the $CaCO_3$ transient precursors. Consistently, in absence of L-Asp, the mineralization process is faster and proceeds through a liquid-liquid binodal separation and the formation of $CaCO_3$ microdroplets that are found enriched in bicarbonates as seen by DNP NMR. Subsequent dehydration

leads to the deposition of ACC nanoparticles. The study of prenucleation stages of mineral formation by the combination of *in situ* LP-TEM, advanced analytical techniques (including hyperpolarized solid-state NMR) and numerical modeling allows the real-time monitoring of prenucleation species formation and evolution and the comprehension of their relative stability.

## Introduction

Biomineralization refers to the ability of living organisms to produce minerals in a controlled manner in their cellular or extracellular matrix. The so-called biominerals are formed from abundant elements in Earth's crust[1] (oxygen, silicon, calcium, iron, etc.) and, often in conjunction with an organic scaffold, provide crucial structural and biochemical functions such as skeletal support, protection or ions storage[2,3]. The phenomenon of biomineralization is witnessed among different species, from marine organisms to mammals. As a proof of diversity of biomineralization, one can cite diatoms in oceans that are able to precipitate silica from their environment to create their ornate frustula[4], magnetotactic bacteria that may produce magnetite which have ferromagnetic properties[5] , shellfish and crustaceans that use calcium carbonate to build efficient and mechanically resistant structures[6]. Last but not least humans and all vertebrates are able to produce hydroxyapatite to form bones and teeth[7].

The biologically controlled production of these minerals occurs in the presence of an organic matrix which templates and directs nucleation and growth[8,9]. The organic matrix comprises a soluble part with macromolecules (proteins, polysaccharides, etc.) regulating the different processes involved in the formation of biominerals, and an insoluble part which acts as a scaffold or template for mineralization (*e.g.* chitin in nacre or collagen in bone)[10]. The organo-mineral interplay leads to the control of composition, size, morphology, orientation and 3D repartition of the biominerals inside the mineralized tissues. As a consequence, the latter exhibits complex architectures associated to multiple properties that surpass those of the analogous synthetically manufactured with similar composition [6]. As a striking example, nacre possesses a 3,000-fold enhanced fracture resistance compared with pure aragonite that is usually brittle and unstable under shear forces[10,11]. What makes biomineralization fascinating for chemists is the ability of living organisms to build such complex structures using naturally-occurring chemicals, at room temperature and in fully aqueous conditions which is much more sustainable than how engineering materials are processed. However, we are still unable to duplicate this remarkable chemistry, the main reason being the fact that the molecular-level mechanisms of biomineralization (in particular, biomolecules/ions association and interaction) are still poorly understood.

Among the various biominerals, calcium carbonate ($CaCO_3$) is extensively studied because of its prevalence in nature, its implication in the $CO_2$ cycle and its high potential in biomimetic applications in industrial and biotechnological fields[12–14]. Numerous studies have shown that the soluble macromolecules involved in $CaCO_3$ mineralization belong to the family of "acidic" proteins (rich in aspartic acid and glutamic acid) which control the nucleation of its different polymorphs as well as the crystal growth, morphology and orientation[15–23].

In order to rationalize the comprehension of these protein interactions, Picker et al.[24] attempted to describe the impact of the constituent amino acids and demonstrated via potentiometric measurements that L-Aspartic acid has the strongest influence on the early stages of $CaCO_3$ mineralization. Recently, an increasing body of experimental evidence[10,25–29] has been pointing towards the existence of intermediate forms of amorphous calcium carbonate (ACC), known as polyamorphism, which are stabilised in the presence of organic additives[30–33]. This biomineralization pathway, where ACC is the transient precursor phase observed before $CaCO_3$ crystallization, is a common strategy used in Nature by several living organisms[25] but differs from classical nucleation pathway[34] where crystals are growing by successive ion addition from supersaturated solutions. In opposition, the existence of unstable transient phases is related to recently described non-classical pathway of nucleation[35–38] where the intermediate phase can be solid or even liquid before transformation into a given crystalline polymorph[39]. Whilst much understanding has been gained on the post nucleation events of calcium carbonate biomineralization and its associated transient phases[40–43], visual insights of the early stages of pre-nucleation are still obscure, and particularly in presence of organic molecules. To rationalize the final and complex properties of biominerals, a clear understanding of these events is crucial. Initial stages of biomineralization, consisting of the prenucleation and nucleation steps, are difficult to analyse with conventional characterization techniques owing to the fact that these events can be particularly fast and elusive. Moreover, a global comprehension of this process requires monitoring and observation of these events in real-time at the molecular level.

In this framework, we tackled the *in-situ* study of pre-nucleation stages of $CaCO_3$ formation by the combination of advanced characterization techniques, namely liquid phase transmission electron microscopy (LP-TEM) and hyperpolarized NMR as a continuity of our previous work on the impact of L-Asp during crystallization of calcium carbonate[44]. *In situ* LP-TEM was already used in the frame of $CaCO_3$ mineralization to observe and determine the pathway of nucleation[45]. It was shown that, in certain conditions, both direct and indirect pathways can coexist including $CaCO_3$ formation both directly from solution and indirectly through transformation of amorphous and crystalline precursors [46]. The role acidic macromolecules in directing mineralization was also explored through *in situ* TEM showing that the binding of calcium ions to polystyrene sulfonate is a key step in the formation of metastable amorphous calcium carbonate[37]. Recently, *in situ* TEM helped in understanding the evolution from ACC to calcite in presence of $Mg^{2+}$ revealing the occurrence of direct transformation without modification of the original morphology of the amorphous state[47]. We note also the study of prenucleation events was also tentatively addressed by *in situ* TEM in the case of calcium phosphate nucleation suggesting that mineralization from simulated body fluid occurs by prenucleation clusters attachment[48]. However, such prenucleation steps were never explored in the case of calcium carbonate through LP-TEM. Importantly, it was recently proposed that the understanding and the control of prenucleation species structure and dynamic could lead to particle-driven mineralization pathways in order to tailor the properties of inorganic functional hybrid materials via structuration from the nano- to the mesoscale[49].

Here we show that LP-TEM allows the identification of prenucleation events as it provides a spatial and time resolved monitoring of the structural evolution of $CaCO_3$ precipitation from the apparition of transient solute species to the nucleation and the growth process[50–52]. In addition, we also show that hyperpolarized solid-state NMR at low temperature (namely, dynamic nuclear polarization DNP NMR) allows the structural characterization of prenucleation species at the molecular level. The vitrification of the solution at a given time point enables the description of the soluble transient precursor by $^{13}C$ DNP MAS NMR before $CaCO_3$ nucleation. Moreover, to obtain a representative insight into the influence of the soluble macromolecules on calcium carbonate mineralization, we focused on the impact of acidic amino acid namely L-Aspartic acid (L-Asp). Indeed, charged polyelectrolytes, in particular polyaspartate, are believed to mimic the action of acidic proteins through a specific association with $Ca^{2+}$ and $CO_3^{2-}$ ions to form an intermediate liquid phase prior to solid nucleation (namely the so-called polymer-induced liquid-precursor PILP process)[13]. The comparison with free-L-Asp solution reveals the influence of charged organic electrolytes onto the successive steps of formation of $CaCO_3$ structures upon non classical pathways of nucleation. As a result, LP-TEM enables the observation of the birth and the evolution of transient phases including prenucleation clusters and liquid dense microdroplets. As a complementary tool, DNP NMR provides crucial atomic details required to understand $CaCO_3$ pathways of formation, that includes the carbonate ions speciation involved into prenucleation species and the binding mode of L-Asp regarding both $Ca^{2+}$ and carbonate ions. Confrontation with DFT calculations helps to understand the mode of operation of L-Asp that allows the regulation and the evolution of prenucleation species up to the solid formation.

## Experimental section

The chemicals were purchased from Sigma-Aldrich and used as received. $^{13}C$-labelled sodium carbonate was obtained by heating sodium bicarbonate (labelled $^{13}C$ – 99%, Cortecnet) at 573K under an inert atmosphere for 2 hours[53]. $^{13}C$-labelled $Na_2CO_3$ purity (<96%) was checked by X-ray diffraction and $^{13}C$ solid-state NMR.

***Mineralization solutions.*** Two stocks solutions were prepared: (1) a 100mM calcium chloride solution and (2) a 10mM sodium carbonate solution mixed or not (reference experiment) with 10 mM of L-Aspartic acid (L-Asp, 98+%).

***In situ TEM.*** 1 µL of carbonate + L-Asp solution was dropped on the observation window of the small bottom disposable SiN chip and let to dry as shown in Figure 1A. The small E-chip used in this study was a commercially available chip (EPB-55DNF-10, Protochips Inc., Raleigh, NC, USA) with a 550 x 550 $\mu m^2$ SiN membrane. The cell was then closed by placing the upper large SiN chip on the bottom chip. The large E-chip used here is the commercially available EPT-55W-10 chip (Protochips Inc., Raleigh, NC, USA). Thereafter, 2.7 µL of calcium chloride solution was flown through the inlet of the Protochips liquid cell holder (Poseidon Select 500, Protochips Inc., Raleigh, NC, USA). Final concentrations in the cell were 100 mM of $Ca^{2+}$ and 1.85 mM of carbonates and 1.85 mM of L-Asp). As soon as the calcium solution was flown through the inlet, the mineralization events were probed in real time using a corrected JEOL 2100F/Cs TEM at 200kV, in

continuous capture mode by a CCD camera. Movies were recorded 10 frames per second and the electron dose was calculated as per the model of Schneider et al.[54] to ensure that the phenomena observed were not beam induced. *In situ* images were either extracted from the *in situ* videos or captured at different intervals during the reaction. The same protocol was applied for the reference experiment without L-Asp for which 1µL of pure carbonate solution were used to dry leading to 3.7 mM of carbonates in the cell.

***Calcium ion potentiometry and pH measurements***. Calcium ion potentiometry and pH measurements were performed using calcium ion-selective electrode (Ca-ISE) (Metrohm No.6.0508.110) and a pH electrode (Metrohm No.6.0508.110) to monitor the calcium potential and the pH over time. The pH electrode was calibrated using pH 4.01, pH 7.00 and pH 9.21 Mettler Toledo standard buffers. The Ca-ISE was calibrated with different solutions of $Ca^{2+}$ (10 mM, 50 mM and 100 mM) buffered at pH 7.4 using TRIS (50 mM) and of defined ionic strength using KCl (150 mM). Both calibration and $Ca^{2+}$ potentiometry measurements were performed at a constant temperature of 300 K using a thermostatic bath. Before and between each measurement, electrodes were washed with acetic acid (0.1 M) and double-distilled water before being recalibrated. The recording of calcium ion potentiometry and pH measurements were controlled using the software Tiamo 2.3 (Metrohm).

The $Ca^{2+}$ complexation by L-Asp was investigated as follows: 100 mL of a $CaCl_2$ solution (100 mM) buffered at pH 7.4 (TRIS 50 mM) and of defined ionic strength (KCl 150 mM) was prepared. Then, both calcium ion potentiometry and pH measurements were started (1 measure per second). After 10 min, 100 mL of L-Asp solution (1.85 mM) were added (molar ratio Ca/L-Asp = 54). After, addition, the pH was quickly corrected to 7.4 by addition of few drops of NaOH. Lower Ca/L-Asp ratio were investigated similarly through the addition of 20 or 33 mM L-Asp to 200 mM $CaCl_2$ solution (Ca/L-Asp = 10 and 6, respectively) in equal volume leading to final concentrations of 100 mM for $CaCl_2$ and 10 or 16.5 mM for L-Asp, respectively. Influence of glycerol was investigated similarly by the addition of a 20 mM L-Asp solution (80% vol. $H_2O$, 20% vol. glycerol) into a 200 mM $CaCl_2$ solution (80% vol. $H_2O$, 20% vol. glycerol). Addition was performed adding equal volumes leading to final concentrations of 100 mM for $CaCl_2$ and 10 mM for L-Asp.

The pH monitoring during $CaCO_3$ mineralization experiments was conducted with identical concentrations as for LP-TEM observations: 26.4 mg of L-Asp and 19.6 mg of $Na_2CO_3$ (39.2 mg in free-L-Asp condition) were placed in a beaker and then dissolved by adding 100 mL of a 100 mM $CaCl_2$ solution. Right after mixing, both L-Asp and $Na_2CO_3$ concentrations were 1.85 mM (3.7 mM for $Na_2CO_3$ in free-L-Asp condition). The pH was monitored every second for 30 minutes.

***$^{43}$Ca solution NMR.*** NMR spectra were recorded for $^{43}$Ca-labelled samples as follows. $^{43}$Ca-labelled solutions were prepared using $^{43}$Ca-labelled $^{43}CaCO_3$ ($^{43}$Ca-62.2% labelled, Cortecnet) as a commercial source. $^{43}CaCO_3$ was first dissolved in HCl (1M). Then, the solution was outgazed through $N_2$ bubbling in order to obtain carbonate-free $^{43}$Ca-labelled $Ca^{2+}$ solution. pH was set to 7.4 using Tris-buffer (100 mM) and a few drops of HCl (1M). Final $Ca^{2+}$ concentrations were set to 7.5 mM by adding double-distilled water. Solid L-Asp (0, 1.5, 2.6, 5.2, 7.5, 10.4 or 26.25 mM) was added to obtain 0, 20, 34.7, 69.3, 100, 138.7 and 350% L-Asp-

$^{43}$Ca-labelled $CaCl_2$ solutions, respectively. Prior $^{43}$Ca solution NMR, each aliquot was pH-corrected with a few drops of NaOH solution (0.1/1M).

All $^{43}$Ca solution NMR spectra were acquired at 23°C on a Bruker AVIII 300 NMR spectrometer operating at 7.05 T (300 MHz proton Larmor frequency, 20.2 MHz $^{43}$Ca Larmor frequency) equipped with a 5 mm Bruker BBFO probe. An internal capillary containing dissolved $D_2O$ was used to ensure proper locking of the signal. One dimensional $^{43}$Ca NMR spectra were acquired using an echo sequence and an averaging of 400 to 480 FIDs with a recycle delay of 2 s.

***$^{13}$C solution NMR.*** The $T_1$ and $T_2$ $^{13}$C relaxation parameters were investigated on pure L-Asp solution (25 mM L-Asp) and in presence of $Ca^{2+}$ (25 mM L-Asp + 75 mM $CaCl_2$; Ca/L-Asp = 3). Concentrations were chosen to induce a 1:1 complexation ratio. The solvent was composed of 90% $H_2O$ and 10% $D_2O$ (to ensure proper locking of the signal). The solutions were then buffered with TRIS (50 mM) and pH was adjusted to 7.4 with HCl/NaOH.

All $^{13}$C solution NMR spectra were acquired at 23°C on a Bruker AVIII 300 NMR spectrometer operating at 7.05 T (300 MHz proton Larmor frequency) equipped with a 5 mm Bruker BBFO probe. An external capillary containing dissolved $D_2O$ was used to ensure proper locking of the signal. One dimensional $^{13}$C NMR spectra were acquired by averaging 32 FIDs with a recycle delay of 90 s. For detection, 30˚flip-angle pulses were applied with a length of 7.9 µs using a power-gated sequence to remove $^{1}$H-$^{13}$C scalar couplings. Prior to Fourier transform, all data were zero filled and apodized using a Gaussian window function. Subsequent to Fourier transform, all data were baseline and phase corrected.

Longitudinal relaxation $T_1$ parameter determination was achieved using a power-gated inversion-recovery scheme. For the carboxylate region, 8 successive FIDs were recorded using the following delays τ: 5 µs, 1, 3, 10, 20, 30, 60 and 120 s. For the aliphatic region, the recycle delay was set to 10 s and 8 successive FIDs were recorded using the following delays τ: 5 µs, 1, 2, 4, 8, 13, 20 and 30 s. $T_1$ values were then extracted by fitting the signal intensity using the following equation:

$I[t]=I[0]+P*\exp(-t/T1)$, where P and I [0] are dimensionless constants.

Transverse relaxation $T_2$ parameter determination was achieved using a power-gated CPMG sequence. $T_2$ values were then extracted by fitting the signal intensity using the following equation:

$I[t]=P*\exp(-t/T2)$, where P is a dimensionless constant.

***$^{13}$C MAS DNP NMR.*** All $^{13}$C DNP MAS NMR experiments were performed on a Bruker 800 MHz DNP NMR spectrometer equipped with a Bruker AVANCE NEO console and a 3.2 mm LT-MAS probe operating at $^{1}$H and $^{13}$C Larmor frequencies of 800.13 and 201.19 MHz respectively. The $^{13}$C chemical shifts were referenced to adamantane. Electronic polarization occurred using a gyrotron 527 GHz as a micro-wave source (125 mA at receptor).

The $CaCO_3$ sample was prepared in order to mimic as close as possible the LP-TEM conditions. The volumes were adjusted to fill a sapphire 3.2 mm rotor (≈ 27 µL). $Ca^{2+}$ solution (100 mM) was prepared dissolving $CaCl_2.2H_2O$ in 70% $D_2O$, 10% $H_2O$ and 20% d5-glycerol. TYINIPol radical (5 mM) was further dissolved in the $Ca^{2+}$ solution. Carbonate (5 or 10 mM) and L-Asp (5 mM) solutions were prepared by dissolving $^{13}C$-labelled $Na_2CO_3$ and ($^{13}C$-labelled 1,4) L-Asp in double distilled water, respectively. Then, NMR rotors were prepared as follows: First, L-Asp solution (10 µL, 5 mM) was placed into a 3.2 mm rotor and evaporated using a heat gun. In parallel, the carbonate solution (10 µL; 5 or 10 mM depending on the addition of L-Asp) was placed into a second rotor and evaporated using a heat gun. Then, 30 µL of a 100 mM $Ca^{2+}$ solution was added to the rotor containing the dried L-Asp and left for dissolution for few minutes. The mixture was then transferred into the rotor containing the dried sodium carbonate and left reacting for 3 minutes before inserting the rotor inside the spectrometer at 100 K. Right after the insertion, the solution is vitrified and the reaction process is quenched and ready for DNP NMR characterization.

The $^{13}C$ CP MAS DNP NMR experiments were optimized on frozen solutions of $^{13}C$-labelled $NaHCO_3$ (20 mM in 70% $D_2O$, 10% $H_2O$ and 20% d5-glycerol + 5 mM TYINIPol) at various pH (6 to 12) by addition of TRIS 50 mM adjusted at the desired pH with NaOH or HCl.

For comparison purpose, $^{13}C$ CP MAS DNP NMR experiments were similarly conducted on pure ($^{13}C$-labelled 1,4) L-Asp (1.85 mM in 20 mM in 70% $D_2O$, 10% $H_2O$ and 20% d5-glycerol + 5 mM TYINIPol). The pH was adjusted to 7 by addition of NaOH.

The $^{13}C$ CP MAS DNP NMR experiments performed at 100 K and A MAS frequency of 8 kHz was used to avoid the overlap of carbonate and bicarbonate resonances with glycerol spinning side bands. A $^{1}H$ 90° pulse of 2.5 µs was first used, followed by a 90% ramped spin locking pulse with a RF magnetic field of 80 kHz. A RF magnetic field of 60 kHz was used as spin locking pulse during the contact time ($t_{CP}$) at the $^{13}C$ resonance frequency. The signal intensity was found to be maximal at $t_{CP}$ = 1 ms for the carbonate and bicarbonate signals. This $t_{CP}$ value was further used for mineralization experiments. 1D $^{13}C$ CP MAS DNP NMR spectra were acquired with a recycle delay of 1-5 s and 64-1024 scans were recorded to reach sufficient signal to noise ratio. Two dimensional $^{1}H$-$^{13}C$ heteronuclear correlation (HetCor) DNP NMR spectra were acquired accumulating 48 $t_1$ increments of 20.82 µs using a DUMBO homonuclear decoupling scheme at an operating $^{1}H$ field of 115 kHz and pure phase spectra were obtained using States-TPPI method. Correct scaling in the $^{1}H$ indirect dimension was obtained multiplying the spectral width by a scaling factor of 0.42.

***Preparation of $CaCO_3$ solid phases.*** Samples without L-Asp ($Na_2CO_3$ 3.7 mM dissolved into $CaCl_2$ 100 mM) and with L-Asp (L-Asp 1.85 mM and $Na_2CO_3$ 1.85 mM dissolved into $CaCl_2$ 100 mM) were left for reacting during 1 hour. Reactions were performed in 100% $H_2O$ and 80% $H_2O$ + 20% glycerol to check the influence of the later additive. Precipitates were filtrated, washed with $H_2O$ and ethanol before drying under vacuum for a few minutes. Dried powders were characterized through X-ray diffraction (XRD) and Fourier-transform infrared spectroscopy (FTIR) to identify $CaCO_3$ polymorphs.

***X-Ray Diffraction.*** Dried powders were packed into PMMA sample holders. XRD experiments were performed using Cu Kα (λ=1.54Å) radiation in a Bruker D8 Advance diffractometer with a Lynx eye detector. The 2θ diffractograms were recorded between 15 and 60° (2θ) with steps of 0.05° and a steep time of 1.5s/step for a total experimental time of 22.5 min. Crystalline phases were identified by comparison with 00-005-0586 and 00-025-0127 PDF cards corresponding to pure calcite and vaterite, respectively.

***Fourier-Transform Infrared Spectroscopy.*** FTIR analysis was performed using a PerkinElmer Spectrum 400. Experiments were carried out by acquiring 4 scans from 550 to 4000 $cm^{-1}$ (1 $cm^{-1}$/step).

***DFT calculations.***

Starting from a 10 Å × 10 Å × 13 Å box in which a molecule of L-Asp, a carbonate anion $CO_3^{2-}$ and a calcium cation $Ca^{2+}$ were initially introduced, 36 $H_2O$ molecules were added and both cell parameters and atomic positions were then relaxed with the VASP (Vienna Ab Initio Simulation Package) code based on the Kohn−Sham Density Functional Theory (DFT) and using a plane-wave pseudopotential approach[55]. The potential energy surfaces were then explored by *ab initio* molecular dynamics at 300 K with time steps set at 1.5 fs. A microcanonical ensemble in the NVT (constant number of molecules, constant volume and constant temperature) approach was used. The local energetical minima found were then optimized at 0 K. It should be noticed that since the negatively charged aspartate form was considered, charge was compensated by protonating a water molecule forming an $H_3O^+$ cation: the $H^+$ moved during the MD, forming preferentially an $HCO_3^-$ anion.

## Results and discussion

**Figure 1** displays the schematic representation of the LP-TEM system used to visualize the different stages of calcium carbonate mineralization. The *in situ* system comprises two silicon chips with overlapping electron transparent silicon nitride membranes (**Fig. 1A**). A restricted amount of solution is confined between the membranes to form a miniaturized cell together with the silicon chips. The *in situ* observations (images and videos) were conducted by focusing the electron beam on the area of interest on the silicon nitride window (**Fig. 1B**). Compared to standard TEM analysis where samples are observed under vacuum, LP-TEM allows observing samples in their native environment without perturbation of nucleation and growth processes.

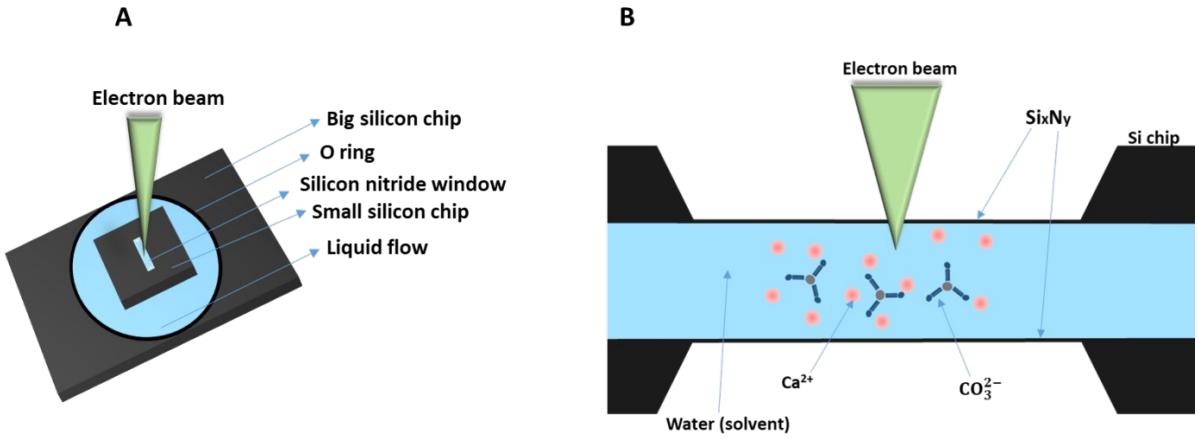



***Figure 1. Schematic representation of the microfluidic liquid cell TEM system****. (A) Top view of a disposable miniaturized liquid cell. (B) Cross sectional view of the liquid cell showing the reaction mixture being irradiated by the electron beam.*

## *In situ formation and dynamics of pre-nucleation species of $CaCO_3$ as visualized by LPTEM.*

In presence of L-Asp, two co-existing stable particle populations were first detected in the reaction medium approximately 3 minutes after the reactants were mixed (**Fig. 2**). Individual nanoclusters were observed (**Fig. 2A-B**) with an average diameter of 1.4 ± 0.3 nm as shown by the size distribution in **Figure 2C.** Their presence is further confirmed by intensity profile analysis (**Fig. S1**) and comparison with blank experiment (pure water) for which the contrast is ~4 times weaker (*i.e.* signal-to-noise-ratio ~4 times lower). According to data reported in literature[35,56] for $CaCO_3$ solutions and according to the size reported here, we assign these individual nanoclusters to pre-nucleation clusters (PNCs) of calcium carbonate stabilized or not by L-Asp (see below).

Interestingly some PNCs further gather to form aggregated nanoclusters with a size ranging between 10 and 20 nm (yellow arrows on **Fig. 2A**). The movie in **SI 2** witnesses the birth of these aggregated nanoclusters which can be discerned by an increasing contrast to form denser aggregates and interestingly with sizes remaining stable during the whole process**.** The series of *in situ* TEM images displayed in **Figure 3** show that the formation of these aggregates (with sizes of 9 and 21 nm in that case) can be completed within ~2 minutes leading to a coexistence with individual nanoclusters (PNCs).

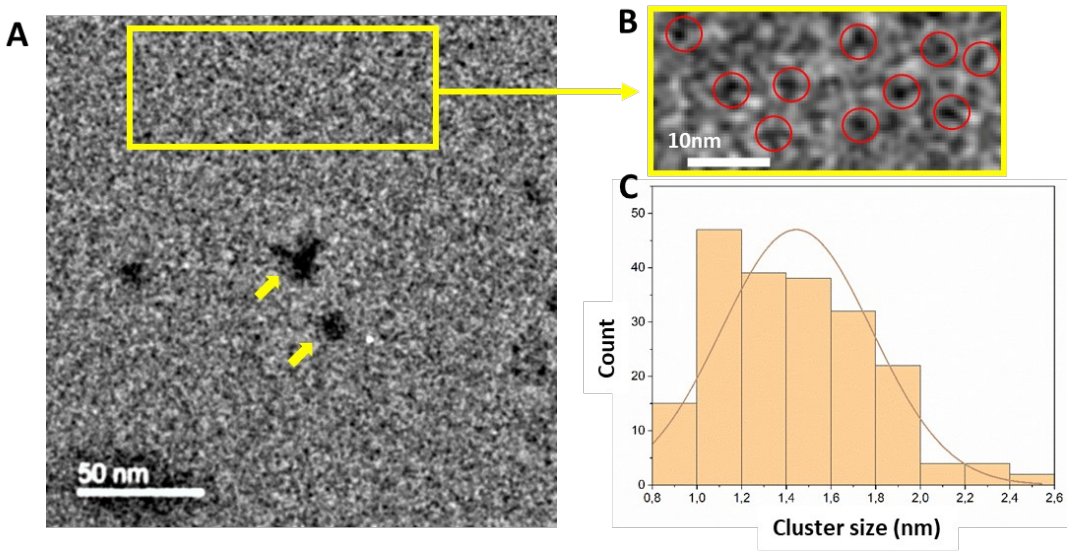



***Figure 2. Observation of individual and aggregated $CaCO_3$ nanoclusters in presence of L-Asp**. (A) In situ LP-TEM image after 3 minutes of reaction displaying individual nanoclusters and aggregated nanoclusters (yellow arrows). (B) Magnification of the demarcated area in (A) showing the individual nanoclusters in red circles. (C) Histogram displaying the size distribution of individual nanoclusters.*

Comparison with literature data help to rationalize our observations. According to their size, the nanocluster aggregates remind the colloidal aggregation of PNCs stabilized by silica[50], questioning the role of L-Asp in our conditions. However, the nanocluster aggregates might be also in line with supramolecular polymers of calcium and carbonate ions stabilized by multiple binding. Simulation studies described that calcium and carbonate ions are linked by ionic bonds with an average coordination number of two. Along the course of nucleation, such polymeric cluster configuration is submitted to a gradual evolution towards denser structures by further ion addition[51].

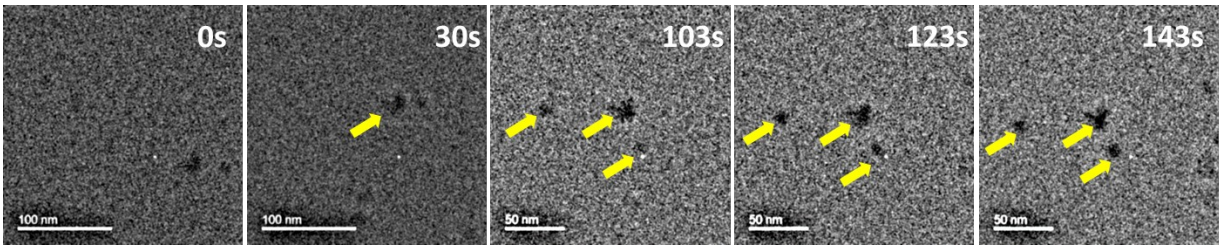



***Figure 3. In situ transformation of individual nanoclusters of $CaCO_3$ towards denser nanocluster aggregates in presence of L-Asp**. The images sequence is acquired by LP-TEM during a time laps of 143 s showing the nanocluster aggregates denoted by the yellow arrows.*

Once formed, these distinct nanocluster aggregates (**Fig. 4A**) were scrutinized for several minutes and, interestingly, we note that their size

(gyration diameter) stay stable with time (**Fig. 4B**), thereby suggesting a thermodynamic equilibrium of such transient species.

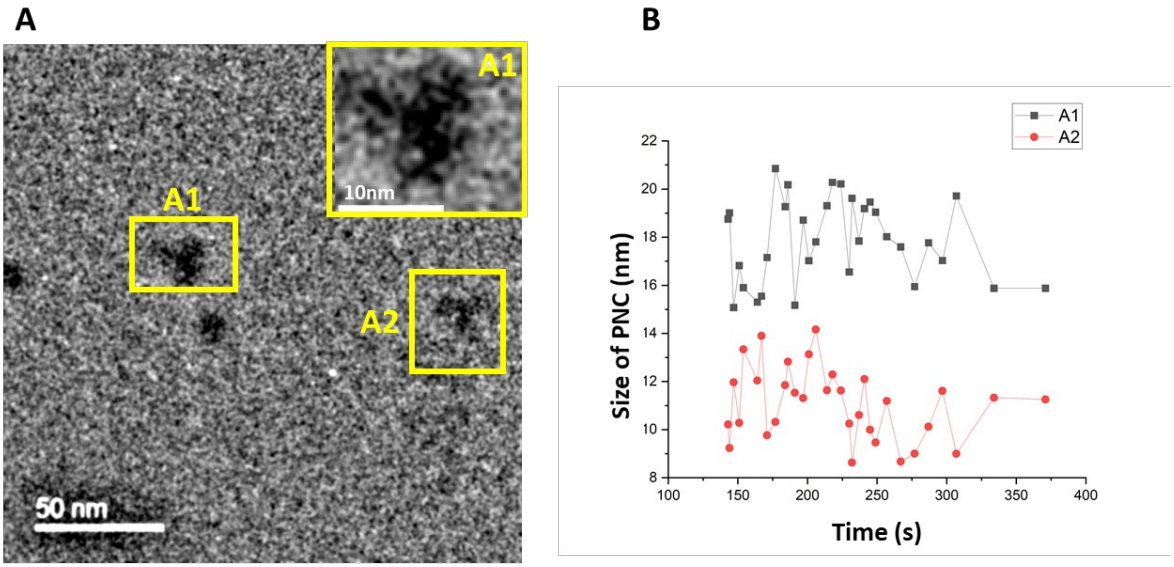



***Figure 4. Size evolution of distinct nanocluster aggregates in presence of L-Asp****. (A) LP- TEM image of nanoclusters aggregates A1 and A2 (yellow rectangles). Yellow inset: close up view of A1 showing the aggregation of individual nanoclusters. (B) Size evolution of A1 and A2 as a function of time.*

**Figure 5** displays a close-up observation for 252s of nanocluster aggregates A1 and reveals the evolution of its morphology. The corresponding images clearly demonstrate that the aggregate is constantly changing its configuration within seconds and therefore exhibits a highly dynamic behaviour. The stability with time of nanocluster aggregates combined with their dynamic configuration remind the salient features of dynamically ordered liquid-like oxyanion polymers (DOLLOP). Previous simulation studies[51] have proposed a DOLLOP-like behaviour of calcium carbonate PNCs where the ions are linked by ionic bonds allowing the molecular precursors chains to behave like a polymer and adopt different dynamic configurations such as rings, linear or branched structures. Due to this rapid exchange of ions and an equilibrium with the solution, there is no phase boundary and hence the PNCs aggregates are considered as solutes within a homogeneous solution. Moreover, MD simulations in combination with quantitative thermodynamic studies[52,57] have demonstrated that during the multiple binding of PNCs, coordinated water is released from the hydration shells of the free $Ca^{2+}$ and $CO_3^{2-}$ ions and the translational and rotational degrees of freedom gained by the water molecules provoke an increase in entropy, rendering the ion association an entropy driven process and not an enthalpy driven reaction. Hence, a DOLLOP-like behaviour is observed experimentally *in situ* even the size observed here are one order of magnitude larger. Interestingly, the presence of L-Asp questions the relative thermodynamic stability observed here and that spans over several minutes. (Figure 4-5). Together with MD simulations[52,57]showing the entropic contribution of the hydrated system it seems that the formation of PNCs can be driven by a general phenomenon occurring in a water-mediated reaction.

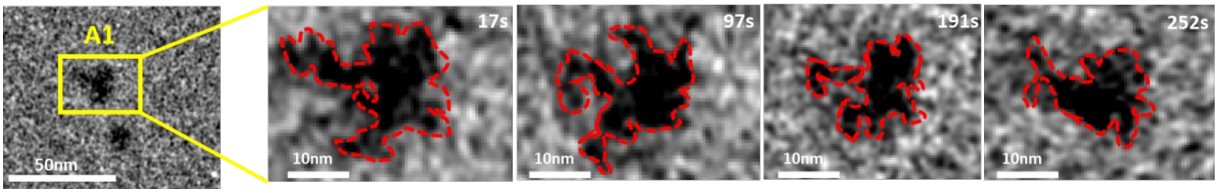



***Figure 5. Dynamics of nanocluster aggregate in presence of L-Asp revealed by LP-TEM****. The distinct nanocluster aggregate A1 is displaying a moving configuration with time (t=0s being the apparition of A1) illustrating the DOLLOP characteristic of PNCs.*

Such nanocluster aggregates are present in the reaction medium for approximately 8 minutes after the mixture of the reactants. Hereafter, a phase transformation occurred causing the disappearance of the pre-nucleation species and the appearance of a solidified phase of different characteristics as detailed in the next section.

### *Real time $CaCO_3$ nucleation through liquid-liquid phase separation.*

The *in situ* LP-TEM images displayed in **Figure 6** and in the movie **SI 3** highlight a phase separation, marking a transition from the pre-nucleation stage to an early post nucleation stage (stage after nucleation and prior to crystallization). Strikingly, we observe that nanocluster aggregates become more defined and less elusive. With time, nanocluster aggregates are seen darker and of fixed conformation losing their highly dynamical behavior (yellow circle in **Fig. 6** and movie in **SI 3).** At the end of the process, aggregates tend to appear in the form of agglomerate of round and denser nanoparticles.

Liquid-liquid phase separation has already been reported during $CaCO_3$ formation[58] but its origin is somehow controversial as it has been proposed to happen directly from free ions in solution[59,60] or through aggregation of PNC. In the latter case, it has been suggested that upon reaching a certain critical limit, the dynamics of the PNCs is greatly reduced, engendering the phase separation[35,36,61]. This phase separation might correspond to a liquid-liquid separation which occurs beyond a binodal limit to form liquid nanodroplets from the PNCs within a dense liquid phase by homogeneous nucleation. The formation of the dense liquid phase is proposed to be more favourable than direct crystallization as the excess free energy of the solid-liquid interface is lower than the solid-crystal interface.[58] Our data (**Fig. 6** and movie in **SI 3**) could be in line with such phase separation and could provide direct visual evidence of liquid nanodroplets. Such individual nanoparticles display an average size of 3,9 ± 0,8 nm and tend to aggregates in 20-50 nm objects.

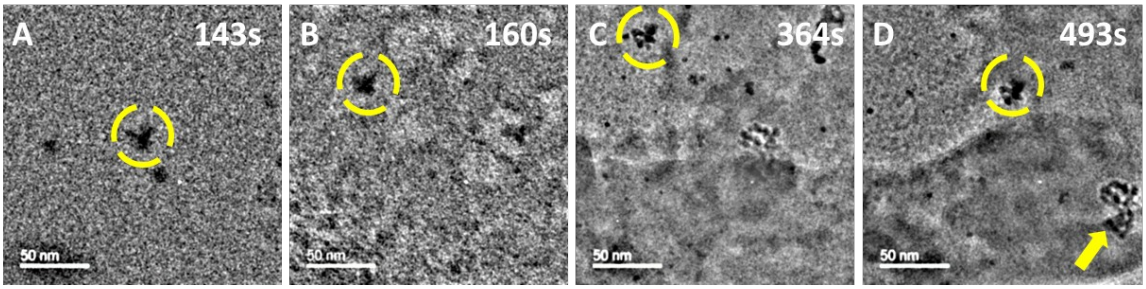



***Figure 6. LP-TEM monitoring of the solidification of PNC aggregates in presence of L-Asp****. (A) TEM image showing the presence of individual nanoclusters and distinct nanocluster aggregates (yellow circle and yellow arrow) prior to phase separation. (B, C, D) Image sequence illustrating the real time formation of a new dense agglomerates of nanoparticles of calcium carbonate.*

In the same time, we observe a phase separation leading to the formation of a dense and extended inorganic network (end of the movie in **SI 3** and movie in **SI 4**). This phenomenon takes the form of a gelification of calcium carbonate-rich network probably driven by water molecules exclusion in which nanodroplets seems to be stuck within.

Then approximately 10 minutes after the complete formation of the dense nanoparticles, the inorganic network is transformed in hydrated ACC nanoparticles probably through drying/annealing process[59]. The ACC nanoparticles are particularly small with a size ranging from 7 to 15 nm and display the tendency to assemble by particle colloidal attachment[62] (**Fig. 7** and movie in **SI 5**) These features question the role of L-Asp as a growth inhibitor.

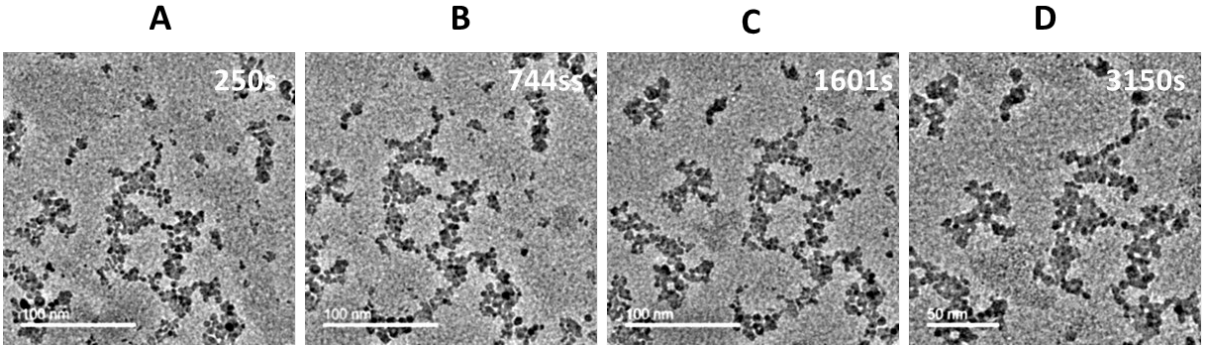



***Figure 7. Stability of ACC nanoparticles in presence of L-Asp****. (A-D) Amorphous calcium carbonate particles assemble by particle colloidal attachment and are stabilized up to almost an hour. (A) is taken 250s after the formation of ACC particles.*

The ACC nanoparticles exhibit a surprisingly long stability with time (almost an hour) probably caused by the crystallization inhibitor nature of L-Asp and hence delaying the crystallization process. The image A of Figure 7 has been taken 250s after the apparition of ACC particles. The comparison with a reference experiment without L-Asp (*vide infra*) evidences this delay in the transformation into ACC highlighting the stabilising role of L-Asp.

### *Calcium carbonate mineralization without L-Aspartic acid.*

To figure out the significance of L-Asp at the incipient stages of calcium carbonate mineralization, we carried out a reference experiment, without the amino acid. The *in situ* TEM image A in **Figure 8** exhibits to the first observation revealing the formation of dense liquid nanodroplets of around 200 to 400 nm 6 min after the mixture of reactants suggesting a binodal separation. With time (~15 min), we observe that their subsequent growth is induced by coalescence leading to microdroplets of several micrometers in size (**Fig. 8A-C** and movie in **SI 6)**. This coalescence does not seem to be due to the displacement of the drops but to the growth of the bigger drops at the expense of the smaller ones (through Ostwald ripening for instance). According to the literature, these dense liquid droplets are rich in calcium carbonate[60]. The formation of dense calcium carbonate-rich droplets was first postulated by Faatz at al.[63] and then observed by Wolf et al. in levitated droplets[58]. The mechanism underlying this process has first been proposed to be related to a liquid-liquid phase separation[64] and later on rationalize as occurring under a binodal separation[59]. It has also been reported by MD simulations[29] that the nucleation of these droplets does not require an energy barrier. Our observations are line with literature data, in particular a liquid-liquid binodal separation leading to $CaCO_3$ nanodroplets of size are in agreement with previous data[58,60]. However, this the first time that the evolution of the $CaCO_3$ droplets are observed *in situ* in particular their growth up to several micrometers through coalescence.

After ~850s $CaCO_3$ micro droplets vanish probably through dehydration and transforms into hydrated amorphous calcium carbonate nanoparticles of sizes ranging from 80 to 150 nm, **(Fig. 8D-F and movie in SI 7)**. Interestingly, the nanoparticles tend to be deposited on the exterior of the former nanodroplets. Hence, the mechanism underlying the deposition of ACC particles seems to be driven by a coffee-ring effect where the evaporation of water molecules occurs from the interior to the exterior of the droplet transporting ACC nanoparticles.

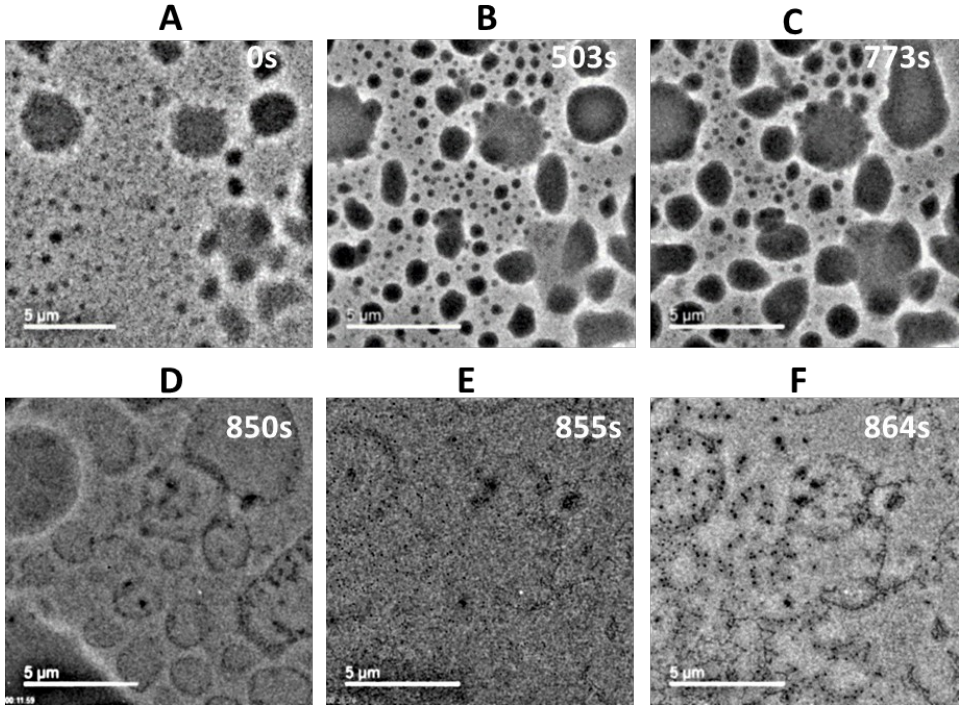


***Figure 8**. **Formation of amorphous calcium carbonate through dense liquid droplets**. (A) Nucleation of dense liquid droplets of ACC. (B, C) Growth of the dense liquid droplets by coalescence and/or Ostwald ripening. (D-F) Transformation of dense liquid droplets into nanoparticles of hydrated ACC.*

The whole process free of L- Asp takes approximately 15 minutes until ACC formation, contrarily to the one with L-Asp which lasted more than an hour. These *in situ* observations provide direct evidence that L-Aspartic acid has a key role in the control of the different stages of $CaCO_3$ mineralization in our conditions.

From a phenomenological point of view, our findings show that the acidic amino acid control prenucleation and nucleation events via a very probable interaction of the L-Aspartic acid with the calcium and carbonate ions present in solution.

### *$Ca^{2+}$-L-Asp interaction in solution.*

To understand $CaCO_3$ formation in presence of L-Asp, $Ca^{2+}$ potentiometric measurements were first carried out as it enables the specific detection of free solute $Ca^{2+}$ and therefore indirectly informs on solute bounded $Ca^{2+}$ in the form of *e.g.* PNCs or complexed calcium ions[34,35,63,64]. In line with the LP-TEM observation conditions (*i.e.* working in excess of Ca with Ca/L-Asp molar ratio = 54), a 100 mM calcium chloride solution was investigated upon dissolution of 1.85 mM of solid L-Asp. Upon L-Asp addition, the detected free $Ca^{2+}$ concentration drop from 100 mM to 98.15 mM and then stabilizes within the 10 following minutes (**Fig. 9A**). Since no precipitation was observed, this drop of 1.85 mM corresponds to $Ca^{2+}$ complexation to L-Asp in a 1:1 ratio. When the Ca/L-Asp molar ratio is decreased to 10 or 6 (still in excess of Ca in order to stay representative of the LP-TEM conditions;), the complexation of $Ca^{2+}$ with L-Asp is still occurring in a 1:1 ratio **(Fig. SI 8)**.

To further understand the $Ca^{2+}$-L-Asp complexation, we recorded $^{43}Ca$ solution NMR spectra from $Ca^{2+}$ solutions (enriched in $^{43}Ca$) of variable L-Asp/Ca ratio including an excess of L-Asp (L-Asp/Ca = 0, 0.2, 0.35, 0.7, 1, 1.4, 3.5). In presence of L-Asp, a single $^{43}Ca$ resonance is observed indicating fast chemical exchange of free and L-Asp-bonded $Ca^{2+}$ at room temperature (**Fig. 9B)**. An asymptotic growth rate of $\nearrow^{43}Ca$ is observed with the increase of L-Asp% tending toward a maximum $\nearrow^{43}Ca$ of 0.27 ppm. We note that at 100% of L-Asp, a plateau is almost reached as the $^{43}Ca$ resonance has shifted from 92% from its initial value (from 0.17 to 0.25 ppm) compared to the maximum (0.27 ppm) (see **Fig. 9C**). The addition of an excess of L-Asp slightly modified the $\nearrow^{43}Ca$ (from 0.25 to 0.27 ppm – 8% of the total shift). This deviation from 1:1 ratio could be explained by a small portion of Ca complexed by 2 L-Asp. However a ratio different from 1:1 is unlikely at low L-Asp/Ca ratio (i.e. in the LP-TEM conditions) as seen by Ca potentiometry. Hence, these results point toward a preferential $COO^-$ complexation site for $Ca^{2+}$ in presence of L-Asp.

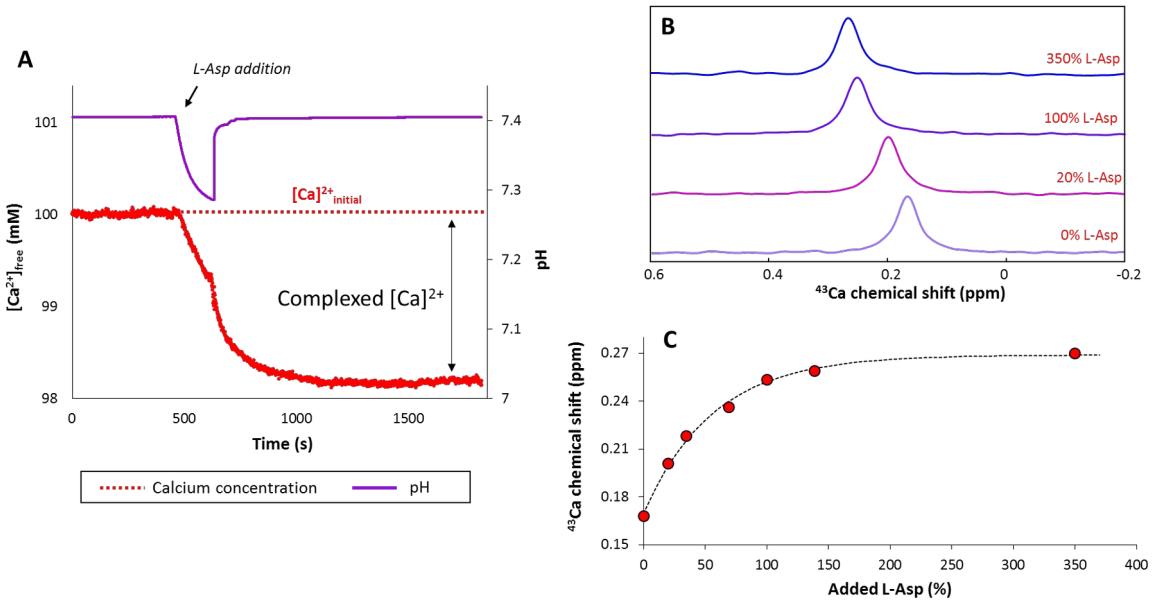



***Figure 9. Calcium complexation to L-Asp through Ca-potentiometry and $^{43}$Ca solution NMR.*** *(A) Dissolution of 1.85 mM of solid L-Asp into 100 mM calcium chloride solution followed by $Ca^{2+}$-potentiometry (red) and pH measurements (purple). (B) $^{43}$Ca NMR spectra of $Ca^{2+}$ solutions (7.5 mM) of various L-Asp amount (0, 20, 100, 350%) (C) Variation of the $^{43}$Ca chemical shift according to the added L-Asp amount.*

## *Structural insights of $CaCO_3$ prenucleation species using MAS DNP.*

In order to get structural insights of transient soluble entities observed by LP-TEM and in particular to highlight the role of L-Asp on the stabilization of prenucleation species, we performed dynamic nuclear polarization (DNP) MAS NMR experiments in order to benefit from two key advantages: (*i*) the increase in NMR sensitivity provided by DNP[67] and (*ii*) the low temperature conditions (100 K). The latter aspect allows to record NMR spectra of frozen solutions and enables the quenching (or the strong reduction) of dynamic in solution. As a result, it becomes possible to characterize by solid-state NMR transient dynamic solute species as shown recently for glycine precipitation[68,69]. Dynamic Nuclear Polarization (DNP) has recently emerged as an appealing technique to drastically enhance the sensitivity of solid-state NMR spectroscopy and, in particular, to amplify signals at surfaces in an approach called DNP SENS (DNP Surface Enhanced NMR Spectroscopy)[70]. If the first proofs of concepts were reported on model mesoporous silica matrices of high surface area[71], recent applications of DNP SENS concern a large range of chemical systems such as high performance organometallic heterogeneous catalysts, doped silicon surfaces, metal-organic frameworks, ligand-capped nanoparticles, cementitious materials, quantum dots or active Sn-zeolites[72]. Here, we expend the use of DNP MAS to more homogeneous systems namely solute pre-nucleation clusters and dense liquid microdroplets.

For pure sodium bicarbonate frozen solution (20 mM, pH 10) an enhancement factor of $\varepsilon_{^{13}C\ CP} \approx 30$ (carbonate resonance) was determined

evidencing the efficiency of NMR signal enhancement from frozen solutions through DNP process under MAS conditions (**Fig. SI 9**). Then, various pH was investigated (from 6 to 12) in order to highlight the possible $CO_3^{2-}/HCO_3^-$ speciation in these conditions (**Fig. SI 10**). As a result, the $^{13}C$ CPMAS DNP NMR spectra display two distinct signals corresponding to carbonates (~168 ppm) and bicarbonates (~161 ppm) of variable proportions according to the initial pH. This feature confirms that working at 100 K leads to quench the fast $CO_3^{2-} \leftrightarrow HCO_3^-$ interconversion and allows the observation of carbonate speciation in frozen solutions. The $CO_3^{2-}$ *vs* $HCO_3^-$ assignment was further confirmed by recording slow $^{13}C$ CPMAS DNP NMR experiments ($\nu_{MAS}$ = 4 kHz; **Fig. SI 11A**) revealing distinct chemical shift anisotropy CSA (*i.e.* distinct spinning sideband patterns). The determination of CSA parameters is in agreement with previous data from the literature[73] as a positive (≈ +66 ppm) and negative (≈ -48 ppm) $\Delta_{CSA}$ values are extracted for bicarbonate and carbonate, respectively (**Fig. SI 11B**). The $CO_3^{2-}/HCO_3^-$ speciation at 100K is influenced both by the low temperature and the partial deuteration as the "apparent" pKa ($HCO_3^-/CO_3^{2-}$) in the DNP conditions is decreased from 10.3 to ~6 (**Fig. SI 10B-C**). Hence, this series of spectra do not reflect the $HCO_3^-/CO_3^{2-}$ absolute proportion at ambient but provides reference $CO_3^{2-}/HCO_3^-$ resonances ratio expected at a given pH in order to understand the speciation evolution during mineralization experiment.

For $CaCO_3$ mineralization experiments in the absence of L-Asp, freshly prepared calcium carbonate solution has been cryo-freezed inside the NMR spectrometer 3 minutes after reaction. According to LP-TEM observations, $CaCO_3$ transient precursors are in the form of dense liquid phase of micrometric size. The corresponding $^{13}C$ CPMAS DNP NMR spectrum displays two distinct signals corresponding to carbonates and bicarbonates **(Fig. 10A**) confirming the potential of DNP NMR to study carbonate species in the context of $CaCO_3$ mineralization and in particular the prenucleation stage. Interestingly, the $CO_3^{2-}/HCO_3^-$ proportion does not match with the expected speciation at pH 8.7 (*i.e.* the pH measured after 3 min of reaction; **Fig. SI 12A**) where bicarbonates should account for ~20% of the signal at 100 K according to the reference experiment (**Fig. SI10A**). In presence of $Ca^{2+}$, the $HCO_3^-$ signal is largely predominant (~60%). This result is not trivial to understand. However, as calcium being in large excess, all carbonates ions mostly reside in the dense liquid phase. Taking into account that the radicals are homogenously dispersed, the $^{13}C$ CPMAS DNP NMR spectrum must be characteristic of the dense liquid phase and suggests that the microdroplets are enriched in $HCO_3^-$ compared to what is expected at pH 8.7. This result is actually consistent with previous $^{13}C$ liquid NMR analyses of 20mM bicarbonate buffer in presence of $CaCl_2$ at pH 8.5[74]. In these conditions, liquid-like droplets of calcium carbonate are formed and the authors demonstrate that such condensed phase is stabilized and enriched in bicarbonate ions compared to the initial solution in absence of calcium. The same process is likely to happen here and might be general for dense liquid phases of $CaCO_3$ for which the local pH inside the microdroplets could be lower than the rest of the solution.

In the presence of L-Asp, PNCs and aggregated PNCs transient species are formed after 3 min of reaction according to LP-TEM observation. The corresponding $^{13}C$ CPMAS DNP NMR spectrum displays both carbonates and bicarbonates and the strong resonance of COO from L-Asp at 176 ppm (**Fig.**

**10B**). The $HCO_3^-/CO_3^{2-}$ proportion (~1:3) observed in the presence of L-Asp is in fairly good agreement with the speciation expected at pH 8 (*i.e*. the pH measured after 3 min of reaction; **Fig. SI 12B**). We do not observe any excess of bicarbonates for these prenucleation species contrary to dense liquid microdroplets (*i.e.* in absence of L-Asp). Hence, in that case the carbonate speciation into PNCs and aggregated PNCs seems to depend directly on the global pH.

The recording of 2D $^1H$-$^{13}C$ heteronuclear correlation (HetCor) spectra is particularly informative on the potential interactions at the molecular level that could take place between the different species in solution. The 2D $^1H$-$^{13}C$ HetCor DNP NMR spectrum of calcium carbonate after 3 min of reaction allows the detailed analysis of the $^1H$-$^{13}C$ correlations involving the $^{13}C$ isotropic resonances of carbonate (167.7 ppm), bicarbonate (161.0 ppm) and glycerol (62.4 and 71.8 ppm) (**Fig. 10C**). As the glycerol used here is d5-Gly ($HOCD_2$-$CD(OD)$-$CD_2OH$), the $^1H$ correlations seen for glycerol correspond to $CD_2OH$ moieties (12.1 ppm) and $H_2O$ in the close coordination sphere of glycerol (5.6 ppm). For carbonates, the main correlation for $CO_3^{2-}$ and $HCO_3^-$ concerns water molecules found around 6.0 ppm, higher than water from glycerol. Dense liquid microdroplets are known to be highly hydrated,[75,59] that could explain the presence of two distinct pools of water molecules solvating carbonates and glycerol, respectively. An additional cross peak is observed for bicarbonates around 11.8 ppm that corresponds to $\mathbf{H}CO_3^-$ [73,76,77] in agreement with the quenching of the fast $CO_3^{2-} \leftrightarrow HCO_3^-$ interconversion at 100K. Hence, this $^1H$ resonance cannot arise solely from OH from glycerol because conversely it would have also been observed for $CO_3^{2-}$ and not only $HCO_3^-$ (see $^1H$ slices extracted from the 2D at the carbonate and bicarbonate position in **Fig. S13a**).

In presence of L-Asp, the 2D $^1H$-$^{13}C$ HetCor DNP NMR spectrum is particularly informative on the L-Asp/carbonates interaction. For a pure L-Asp solution, the 2D $^1H$-$^{13}C$ HetCor DNP NMR spectrum (**Fig. S14**) displays distinct correlation signals for glyclerol and L-Asp. For L-Asp, $^1H$ correlation peaks with 1,4 COO groups (~177 ppm) are seen at 3.6 ppm ($CH_2$/CH) and 12.8 ppm ($NH_3$). For d5-glycerol, the $^1H$ correlation peaks are still displayed at 5.6 ($H_2O$) and 12.1 ppm ($CD_2OH$). According to the 2D HetCor and the extracted $^1H$ slices at the L-Asp and glycerol position, the two additives seem to not interact significantly at the molecular level. In the case of $CaCO_3$ mineralization in presence of L-Asp (**Fig. 10D)**, the $CO_3^{2-}$ resonance exhibits a correlation at 12.6 ppm (not present without L-Asp) suggesting an interaction at the molecular level with NH from L-Asp. For bicarbonates, similar conclusion is not straightforward because the correlation is weaker and might also contain contribution of protons from bicarbonate.

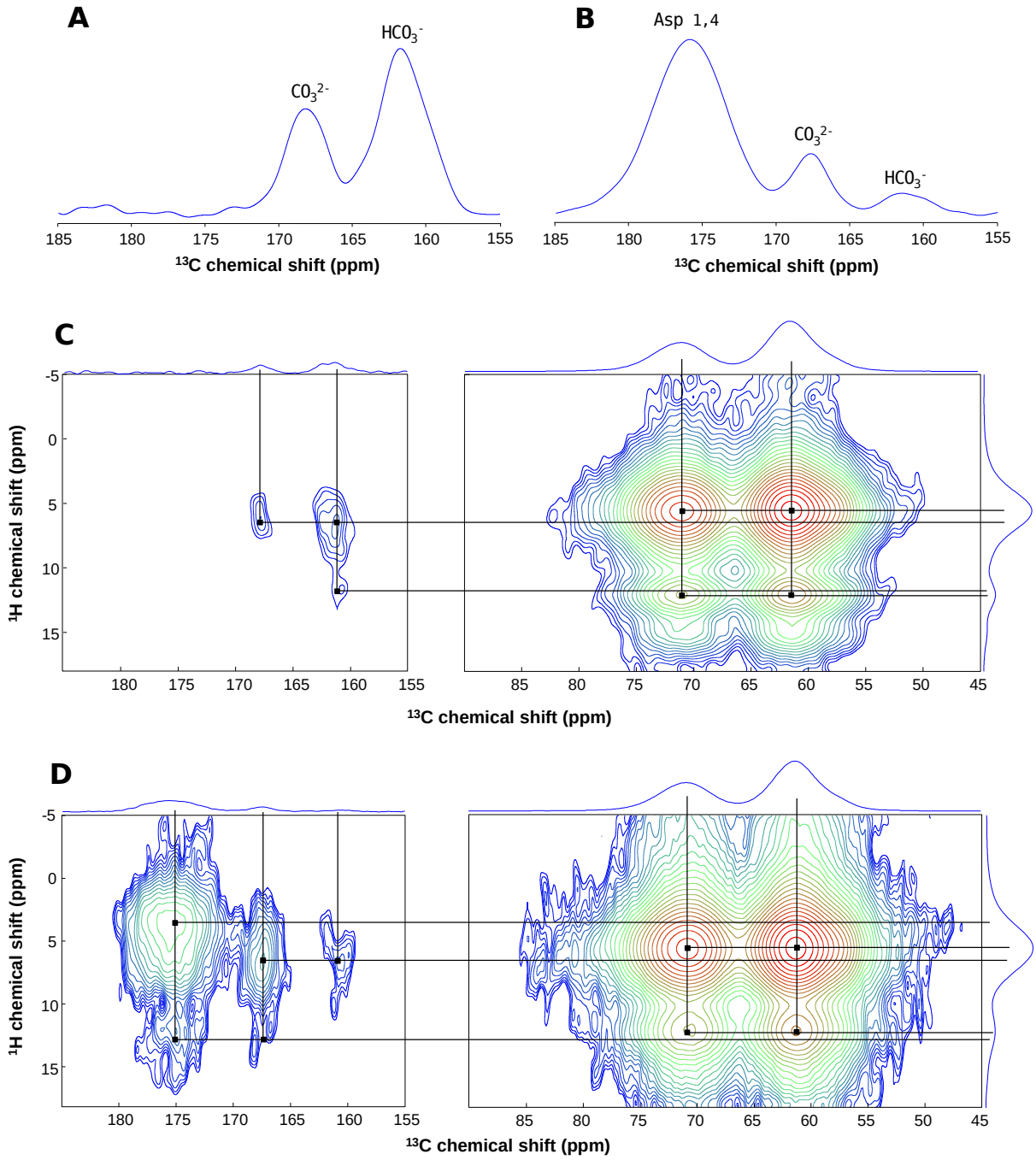



***Figure 10. Carbonate speciation into $CaCO_3$ precursors through $^{13}C$ DNP MAS NMR.*** *$^{13}C$ CPMAS DNP NMR spectra of calcium carbonate solution without (A) and with (B) L-Asp after 3 minutes of induction time. $^{1}H$-$^{13}C$ HetCor DNP MAS spectra of calcium carbonate solution without (C) and with (D) L-Asp frozen still after 3 minutes of induction time.*

Glycerol seems not to interact significantly with L-Asp/$CO_3^{2-}$/$HCO_3^-$ at the molecular level. This finding is reinforced by Ca-potentiometry showing that addition of 20% glycerol does not change the expected $Ca^{2+}$ concentration and does not modify the binding capacity of L-Asp toward $Ca^{2+}$ (**Fig. S15**). However, even in absence of molecular level interaction, the modification of the solvent properties can influence the course of the precipitation events. To dismiss such hypothesis, XRD and FT-IR analysis were undertaken and show that the final

calcium carbonate products are in similar in terms of composition (vaterite and calcite) and proportion upon addition of 20% glycerol (**Fig. S16**). These findings are in agreement with the charges carried out by the electrolytes imposed by the pH of the solutions (*i.e.* $^{-}OOC\text{-}CH_2\text{-}CH(NH_3^+)\text{-}COO^-$, $CO_3^{2-}/HCO_3^-$ and $Ca^{2+}$) for which the main interactions seem to be driven by electrostatic forces. In that case, the interactions detected by DNP MAS NMR experiments seem to be representative of the L-Asp/carbonates interplay in prenucleation species. Taking into account Ca-potentiometry and $^{43}Ca$ NMR, these results plead for a complexation of the $Ca^{2+}\text{-}CO_3^{2-}$ and $Ca^{2+}\text{-}HCO_3^-$ ion pairs by L-Asp through $COO^-$ and $NH_3^+$ moieties.

To go deeper in the comprehension of calcium complexation by L-Asp, small models were elaborated in a cell of 1.17 $nm^3$ where L-Asp is microsolvated (36 water molecules). At our working pH (~8) and according to their respective pKa (2.0, 3.9 and 10.0,) the two carboxyl groups are deprotonated whereas the amine is protonated: $^{-}OOC\text{-}CH_2\text{-}CH(NH_3^+)\text{-}COO^-$. When $Ca^{2+}$ and $CO_3^{2-}$ are positioned close to $C_1$ or $C_4$ and the charge compensated by protonating a water molecule forming an $H_3O^+$ cation, we observe a spontaneous protonation of $CO_3^{2-}$ forming a $HCO_3^-$ anion. This protonation prevents the numerical study of $CO_3^{2-}$ in these conditions. However, the evolution of the system in presence of bicarbonate is particularly informative. Indeed, a stable conformation is observed which is characterized by a complexation of the $Ca^{2+}\text{-}HCO_3^-$ ion pairs by L-Asp through $C_1OO^-$ and $NH_3^+$ moieties (**Fig. 11**). In this configuration, two of the $HCO_3^-$ oxygens are linked to $Ca^{2+}$ with Ca—O distances ~ 2.5 Å while one of the $HCO_3^-$ oxygens is also H-bonded to $NH_3^+$. Another conformation, although slightly less stable, shows only one $HCO_3^-$ oxygen linked to $Ca^{2+}$ and a different oxygen H-bonded to $NH_3^+$ (**Fig. SI 17B**). Complexation by $C_4$ seems less favorable (**Fig. SI 17C**) as well as bidentate complexation of calcium ion to $C_1$ carboxylate oxygens (**Fig. SI 17D**). Nonetheless, a more detailed DFT study would be necessary to confirm these results in terms of relative energies from one configuration to the other. All in all, modeling shows that complexation of the $Ca^{2+}\text{-}$ $HCO_3^-$ ion pairs by L-Asp is definitely reasonable. However, and very importantly, the size of the formed complexes (~1.1 nm) are in the same range as the PNC (~1.4 nm) observed by LP-TEM at the very first stage of $CaCO_3$ mineralization in presence of L-Asp suggesting that individual PNC are $Ca^{2+}$—$CO_3^{2-}/HCO_3^-$ ion pairs stabilized through L-Asp complexation.

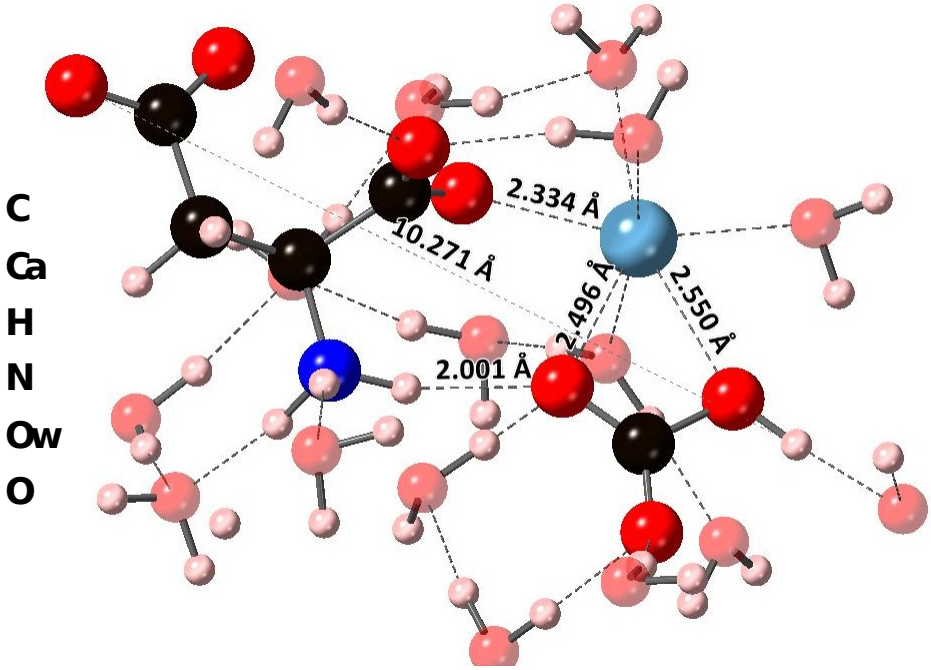



***Figure 11.*** *Low energy configuration obtained by DFT for microsolvated L-Asp in interaction through C1OO$^-$ and $NH_3^+$ with $Ca^{2+}$ and $HCO_3^-$. Characteristic distances are shown*

Our results are in agreement with recent MD simulations showing that complexation of calcium ion to carboxylate oxygens is favored for acetate and glycine in aqueous environment [78]. Hence, L-Asp seems to regulate the presence of PNC and aggregated PNC in water through a double organic-inorganic interaction involving both the $COO^-$ groups and the $NH_3^+$ to attract $Ca^{2+}$ and $CO_3^{2-}/HCO_3^-$, respectively, leading to nanometric entities observed in LP-TEM at beginning of the mineralization process. Moreover, the strong affinity of aspartate for calcium carbonate was also shown through the use of L- and D-Asp to grow left- and right-handed vaterite toroids, respectively[79]. The growth of these toroids appears to be enabled by the formation of homochiral clusters of aspartic acid at the vaterite surface[80]. It is also important to note that once the $CaCO_3$ crystallization is achieved, it has been shown that L-Asp can be trapped within the crystalline lattice of vaterite or calcite resulting in occlusions for which two sets of interfacial carbonates have been evidenced on the basis of their respective carbonate-amine distances (~3.8 and >5Å) [81]. Hence, we cannot exclude the incorporation of L-Asp inside our final $CaCO_3$ products.

To identify the most favorable complexation site, we performed longitudinal relaxation $T_1(^{13}C)$ measurements on L-Asp solutions with and without calcium ions (**Fig. SI 18A**). It was shown that $T_1(^{13}C)$ parameters of amino acids decreases when complexing with some metallic cations such as $Ca^{2+}$ or $Mg^{2+}$ [82,83]. Interestingly, carbon $C_1$ is the most impacted by a $T_1$ decrease (-47.5%) compared to carbon $C_4$ (-30.2 %) (Aliphatic $C_2$ and $C_3$ carbons are the least affected with a $T_1$ decrease of 21.7 and 3.1%, respectively). A similar trend is observed for spin-spin relaxation $T_2(^{13}C)$ measurements. In presence of L-Asp, $C_1$ carbon is the most affected by a $T_2$ decrease (-86.1%) (**Fig. SI 18B**). These

results might suggest $C_1$ as the preferential complexation site for calcium. However, the identification of $Ca^{2+}$ complexation site based on $T_1$, $T_2$ measurements and MD calculations is still not univocal.

### *The relevance of L-Aspartic acid at the incipient stages of calcium carbonate mineralization*

Gebauer et al. categorized the inhibiting effects of additives on calcium carbonate mineralization into seven types[84]. According to our main findings, we can assume that L-Asp has the following types of inhibition on calcium carbonate:

- Type I: adsorption of calcium ions
- Type II: influence of soluble cluster formation and equilibria
- Type III: Inhibition of nucleation of a precipitated nanoparticle phase
- Type IV: Adsorption on nucleated particles and their stabilization

The complexation of L-Aspartic acid with the ions via the amine and carboxyl groups, controls the mineralization by favoring the formation et stabilization of pre-nucleation clusters as illustrated in **Figure 12**.

Besides, it seems interesting to us to establish a certain parallel between the mechanisms associated with biomineralization processes leading to the formation of calcium carbonate in the presence of a complexing agent such as aspartic acid and the formation of metal-oxo polymers and metal oxides obtained by sol-gel chemistry in the presence of inhibiting agents[85-88].

Indeed, the general behavior of calcium carbonate in presence of the complexing L-Asp molecule prior to crystallization during biomineralization in the amorphous domain is congruent with that of inorganic or hybrid materials produced via chimie douce as nano-scaled colloids, gels or precipitates. The synthesis of these hybrid colloids starts with hydrolysable metallo-organic precursors which reactivity is controlled by adjusting pH or by adding complexing ligands[89-91]. These chemical additives slow down condensation reactions, inhibit the crystallization and therefore favor the formation of small soluble metal-oxo clusters (analogue to PNC) in" pseudo equilibrium" with amorphous metal-oxo polymers. During the first steps and depending on concentration of precursors these amorphous oxo-polymers produces bushy amorphous structures which invade the whole volume of the resultant nanocolloids or gels (analogue to DOLLOP). Solvent, reaction by products and residual metal-oxo clusters being trapped inside the bushy amorphous network[92-94]. The latter controls the final properties of the materials by adopting different structures according to the chemical and processing conditions. At longer times the clusters feed the metal-oxo polymers to produce more robust amorphous networks which can be transformed in a last processing step into crystalline metal oxides[93,95]. So, in some way the demeanor of calcium carbonate with L-Asp can be assimilated to that of precursors of sol gel chemistry to form inorganic materials.

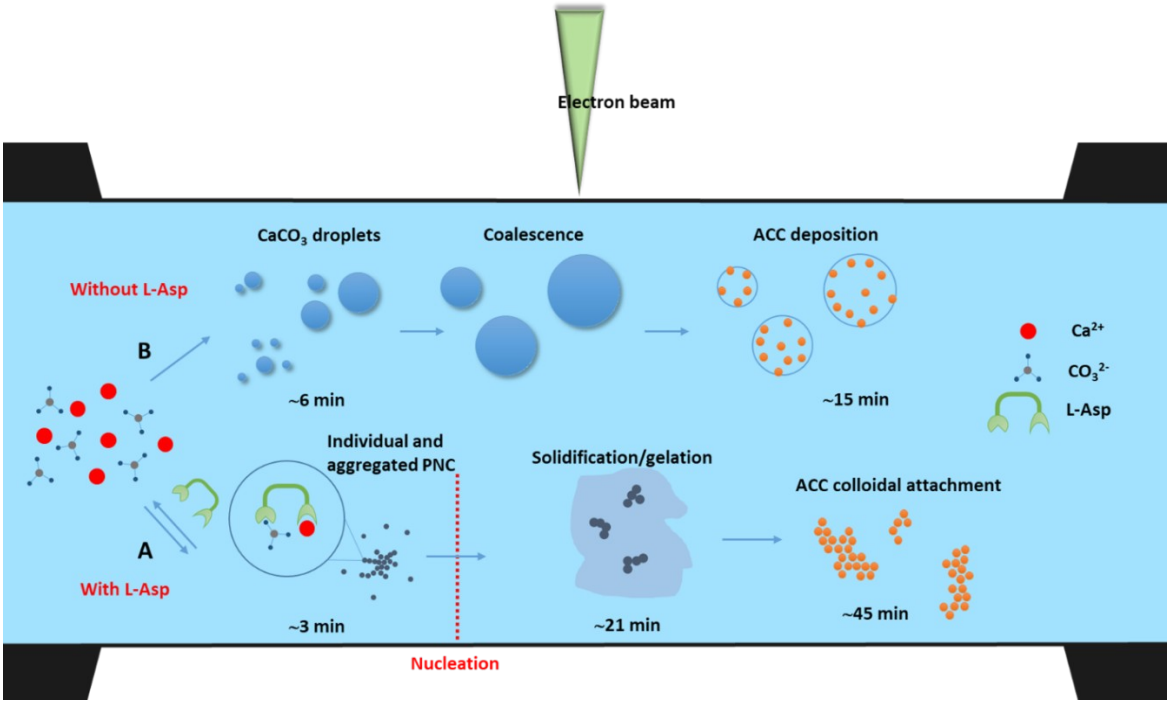



***Figure 12. Schematic sequence illustrating $CaCO_3$ mineralization in presence and absence of L-Asp.*** *The presence of L-Asp in solution promotes and stabilizes pre-nucleation clusters in solution through specific carbonate/$Ca^{2+}$ interaction. Next, nucleation occurs through the fast reduction of the dynamic including formation of nanodroplets or particles through PNC dehydration and gelation of calcium carbonate-rich network. Then, nanoparticles of hydrated ACC are precipitated with sizes controlled by L-Asp. Without ACC, liquid-liquid bimodal separation is occurring leading to the formation of $CaCO_3$-rich droplets that are growing up mainly through coalescence. Dehydration of induces the precipitation of hydrated ACC nanoparticles within droplets.*

## Conclusions

In conclusion, by using real-time LP-TEM observations in combination with hyperpolarized solid state NMR, we contribute to better establish a mechanistic picture of the role of L-Aspartic acid on the prenucleation and nucleation of calcium carbonate from a phenomenological point of view. The *in situ* formation and stabilization of PNCs and their DOLLOP-like characteristics in presence of L-Asp can be evidenced experimentally by LP-TEM. L-Asp has a fundamental impact on the $CaCO_3$ nucleation pathway as a totally different sequence of events is observed in its absence. In this latter case, nucleation is occurring through a liquid-liquid phase separation and dense microdroplets are observed by LP-TEM. In addition, by using Ca-potentiometry and $^{13}C$ DNP MAS NMR we show the complexing behavior of L-Asp towards calcium and carbonate ions. DFT calculations are in good agreements with $^{13}C$ DNP MAS NMR experiments and suggest that prenucleation clusters are stabilized by L-Asp and consist of $Ca^{2+}$—$CO_3^{2-}$/$HCO_3^-$ ion pairs interacting with carboxylate and ammonium functions. In absence of L-Asp, $^{13}C$ DNP MAS NMR experiments reveal that dense liquid microdroplets are enriched with bicarbonate ions compared to the rest of the

solution. This strong interaction is delaying $CaCO_3$ nucleation compared to free amino acid condition. It is also promoting the transition through a gel-phase and is inhibiting the subsequent growth of ACC nanoparticles. These phenomena are not without reminding those which manage the growth of mineral gels based on metal oxides in the presence of organic complexing inhibitors. This study has highlighted that the combination of LPTEM and low temperature hyperpolarized NMR is a powerful tool to elucidate nanoscale phenomena at the very first steps of mineralization and in particular the influence of complexing amino acid upon nucleation. This approach might be generalized to bigger complexing system such as polyaspartate.

(1) Weiner, S. (2003). An Overview of Biomineralization Processes and the Problem of the Vital Effect. Reviews in Mineralogy and Geochemistry, 54(1), 1–29.
(2) Yao, S., (2017). Biomineralization: From Material Tactics to Biological Strategy. Advanced Materials, 29(14), 1605903.
(3) Biomineralization and Biomimetic Materials Processing. (2016). Biomimetic Principles and Design of Advanced Engineering Materials, 271–297.

(4) Ehrlich, H., & Witkowski, A. (2015). Biomineralization in Diatoms: The Organic Templates. Evolution of Lightweight Structures, 39–58.
(5) Mann, S., Archibald, D. D., Didymus, J. M., Heywood, B. R., Meldrum, F. C., & Wade, V. J. (1992). Biomineralization: Biomimetic Potential at the Inorganic-Organic Interface. MRS Bulletin, 17(10), 32–36.
(6) Weiner, S., & Addadi, L. (2011). Crystallization Pathways in Biomineralization. Annual Review of Materials Research, 41(1), 21–40.
(7) Yun, J., Holmes, B., Fok, A., & Wang, Y. (2018). A Kinetic Model for Hydroxyapatite Precipitation in Mineralizing Solutions. Crystal Growth & Design, 18(5), 2717–2725.
(8) Dhami, N. K., Reddy, M. S., & Mukherjee, A. (2013). Biomineralization of calcium carbonates and their engineered applications: a review. Frontiers in Microbiology, 4.
(9) Tavafoghi, M.; Cerruti, M. The Role of Amino Acids in Hydroxyapatite Mineralization. J. R. Soc. Interface 2016, 13 (123), 20160462.
(10) Gajjeraman, S., Narayanan, K., Hao, J., Qin, C., & George, A. (2006). Matrix Macromolecules in Hard Tissues Control the Nucleation and Hierarchical Assembly of Hydroxyapatite. Journal of Biological Chemistry, 282(2), 1193–1204.
(11) Falini, G., Fermani, S., & Goffredo, S. (2015). Coral biomineralization: A focus on intra-skeletal organic matrix and calcification. Seminars in Cell & Developmental Biology, 46, 17–26.
(12) Hamm, L. M. (2012). Calcium Carbonate Biomineralization: A Theoretical and Experimental Investigation of Biomolecular Controls on Nucleation and Growth. Faculty of the Virginia Polytechnic Institute.
(13) Gower, L. B. (2008). Biomimetic Model Systems for Investigating the Amorphous Precursor Pathway and Its Role in Biomineralization. Chemical Reviews, 108(11), 4551–4627.
(14) Seto, J., & Romero, P. A. (2016). Shaping it up. Biomineralization and Biomaterials, 3–50.
(15) Veis, A., & Dorvee, J. R. (2012). Biomineralization Mechanisms: A New Paradigm for Crystal Nucleation in Organic Matrices. Calcified Tissue International, 93(4), 307–315.
(16) De Yoreo, J. J. (2007). Biomolecular Modification of Inorganic Crystal Growth. AIP Conference Proceedings.
(17) Dalbeck, P., England, J., Cusack, M., Lee, M. R., & Fallick, A. E. (2006). Crystallography and chemistry of the calcium carbonate polymorph switch in M. edulis shells. European Journal of Mineralogy, 18(5), 601–609.
(18) Demichelis, R., Schuitemaker, A., Garcia, N. A., Koziara, K. B., De La Pierre, M., Raiteri, P., & Gale, J. D. (2018). Simulation of Crystallization of Biominerals. Annual Review of Materials Research, 48(1), 327–352.
(19) Dickinson, S. R., Henderson, G. E., & McGrath, K. M. (2002). Controlling the kinetic versus thermodynamic crystallisation of calcium carbonate. Journal of Crystal Growth, 244(3-4), 369–378.
(20) Marin, F., & Luquet, G. (2007). Unusually Acidic Proteins in Biomineralization. Handbook of Biomineralization, 273–290.
(21) Addadi, L., Moradian, J., Shay, E., Maroudas, N. G., & Weiner, S. (1987). A chemical model for the cooperation of sulfates and carboxylates in calcite

crystal nucleation: Relevance to biomineralization. Proceedings of the National Academy of Sciences, 84(9), 2732–2736.
(22) Kretsinger, R. H. (2013). Calcium-Binding Proteins, Overview. Encyclopedia of Metalloproteins, 521–536.
(23) Evans, J. (2017). Polymorphs, Proteins, and Nucleation Theory: A Critical Analysis. Minerals, 7(4), 62.
(24) Picker, A., Kellermeier, M., Seto, J., Gebauer, D., & Cölfen, H. (2012). The multiple effects of amino acids on the early stages of calcium carbonate crystallization. Zeitschrift Für Kristallographie - Crystalline Materials, 227(11), 744–757.
(25) Addadi, L., Raz, S., & Weiner, S. (2003). Taking Advantage of Disorder: Amorphous Calcium Carbonate and Its Roles in Biomineralization. Advanced Materials, 15(12), 959–970.
(26) Cartwright, J. H. E., Checa, A. G., Gale, J. D., Gebauer, D., & Sainz-Díaz, C. I. (2012). Calcium Carbonate Polyamorphism and Its Role in Biomineralization: How Many Amorphous Calcium Carbonates Are There? Angewandte Chemie International Edition, 51(48), 11960–11970.
(27) Koga, N., Nakagoe, Y., & Tanaka, H. (1998). Crystallization of amorphous calcium carbonate. Thermochimica Acta, 318(1-2), 239–244.
(28) Akiva-Tal, A., Kababya, S., Balazs, Y. S., Glazer, L., Berman, A., Sagi, A., & Schmidt, A. (2011). In situ molecular NMR picture of bioavailable calcium stabilized as amorphous CaCO3 biomineral in crayfish gastroliths. Proceedings of the National Academy of Sciences, 108(36), 14763–14768.
(29) Bushuev, Y. G., Finney, A. R., & Rodger, P. M. (2015). Stability and Structure of Hydrated Amorphous Calcium Carbonate. Crystal Growth & Design, 15(11), 5269–5279.
(30) Zou, Z., Bertinetti, L., Politi, Y., Fratzl, P., & Habraken, W. J. E. M. (2017). Control of Polymorph Selection in Amorphous Calcium Carbonate Crystallization by Poly (Aspartic Acid): Two Different Mechanisms. Small, 13(21), 1603100.
(31) Štajner, L., Kontrec, J., Njegić Džakula, B., Maltar-Strmečki, N., Plodinec, M., Lyons, D. M., & Kralj, D. (2018). The effect of different amino acids on spontaneous precipitation of calcium carbonate polymorphs. Journal of Crystal Growth, 486, 71–81.
(32) Gong, Y. U. T., Killian, C. E., Olson, I. C., Appathurai, N. P., Amasino, A. L., Martin, M. C., … Gilbert, P. U. P. A. (2012). Phase transitions in biogenic amorphous calcium carbonate. Proceedings of the National Academy of Sciences, 109(16), 6088–6093.
(33) Yamazaki, T., Kimura, Y., Vekilov, P. G., Furukawa, E., Shirai, M., Matsumoto, H., … Tsukamoto, K. (2017). Two types of amorphous protein particles facilitate crystal nucleation. Proceedings of the National Academy of Sciences, 114(9), 2154–2159.
(34) Gebauer, D., Völkel, A., & Cölfen, H. (2008). Stable Prenucleation Calcium Carbonate Clusters. Science, 322(5909), 1819–1822.
(35) Gebauer, D., Kellermeier, M., Gale, J. D., Bergström, L., & Cölfen, H. (2014). Pre-nucleation clusters as solute precursors in crystallisation. Chem. Soc. Rev., 43(7), 2348–2371.
(36) Gebauer, D. (2018). How Can Additives Control the Early Stages of Mineralisation? Minerals, 8(5), 179.

(37) Smeets, P. J. M., Cho, K. R., Kempen, R. G. E., Sommerdijk, N. A. J. M., & De Yoreo, J. J. (2015). Calcium carbonate nucleation driven by ion binding in a biomimetic matrix revealed by in situ electron microscopy. Nature Materials, 14(4), 394–399.
(38) De Yoreo, J. J. (2003). Principles of Crystal Nucleation and Growth. Reviews in Mineralogy and Geochemistry, 54(1), 57–93.
(39) De Yoreo, J. J., Wang, W., Tsukamoto, K., & Wu, D. (2010). Physical Mechanisms of Crystal Growth Modification by Biomolecules.
(40) Nielsen, M. H., & De Yoreo, J. J. (n.d.). Liquid Cell TEM for Studying Environmental and Biological Mineral Systems. Liquid Cell Electron Microscopy, 316–333.
(41) De Jonge, N., Browning, N. D., Evans, J. E., Chee, S. W., & Ross, F. M. (n.d.). Resolution in Liquid Cell Experiments. Liquid Cell Electron Microscopy, 164–188.
(42) Demmert, A. C., Dukes, M. J., Pohlmann, E., Patel, K., Cameron Varano, A., Sheng, Z., … Kelly, D. F. (n.d.). Visualizing Macromolecules in Liquid at the Nanoscale. Liquid Cell Electron Microscopy, 356–370.
(43) Loste, E., Park, R. J., Warren, J., & Meldrum, F. C. (2004). Precipitation of Calcium Carbonate in Confinement. Advanced Functional Materials, 14(12), 1211–1220.
(44) Longuinho, M., Ramnarain, V., Ortiz Peña, N., Ihiawakrim, D., Soria-Martínez, R., Farina, M., Ersen, O., and André L. Rossi (2022). The influence of L-aspartic acid on calcium carbonate nucleation and growth revealed by in situ liquid phase TEM. CrystEngComm, 24, 2602-2614
(45) De Yoreo, J. J. (2016). In - situ liquid phase TEM observations of nucleation and growth processes. Progress in Crystal Growth and Characterization of Materials, 62(2), 69–88.
(46) Nielsen, M. H., Aloni, S., & De Yoreo, J. J. (2014). In situ TEM imaging of CaCO3 nucleation reveals coexistence of direct and indirect pathways. Science, 345(6201), 1158–1162.
(47) Liu, Z., Zhang, Z., Wang, Z., Jin, B., Li, D., Tao, J., … De Yoreo, J. J. (2020). Shape-preserving amorphous-to-crystalline transformation of CaCO3 revealed by in situ TEM. Proceedings of the National Academy of Sciences, 201914813.
(48) Wang, X., Yang, J., Andrei, C. M., Soleymani, L., & Grandfield, K. (2018). Biomineralization of calcium phosphate revealed by in situ liquid-phase electron microscopy. Communications Chemistry, 1(1).
(49) Gebauer, D., & Wolf, S. E. (2019). Designing solid materials from their solute state: a shift in paradigms towards a holistic approach in functional materials chemistry. Journal of the American Chemical Society, 141, 4490−4504
(50) Kellermeier, M., Gebauer, D., Melero-García, E., Drechsler, M., Talmon, Y., Kienle, L., … Kunz, W. (2012). Colloidal Stabilization of Calcium Carbonate Prenucleation Clusters with Silica. Advanced Functional Materials, 22(20), 4301–4311.
(51) Demichelis, R., Raiteri, P., Gale, J. D., Quigley, D., & Gebauer, D. (2011). Stable prenucleation mineral clusters are liquid-like ionic polymers. Nature Communications, 2(1).

(52) Kellermeier, M., Raiteri, P., Berg, J. K., Kempter, A., Gale, J. D., & Gebauer, D. (2016). Entropy Drives Calcium Carbonate Ion Association. ChemPhysChem, 17(21), 3535–3541.
(53) Dal Pozzo, A., Moricone, R., Tugnoli, A., & Cozzani, V. (2019). Experimental Investigation of the Reactivity of Sodium Bicarbonate towards Hydrogen Chloride and Sulfur Dioxide at Low Temperatures. Industrial & Engineering Chemistry Research. 58, 6316−6324.
(54) Schneider, N. M., Norton, M. M., Mendel, B. J., Grogan, J. M., Ross, F. M., & Bau, H. H. (2014). Electron–Water Interactions and Implications for Liquid Cell Electron Microscopy. The Journal of Physical Chemistry C, 118(38), 22373–22382.
(55) Kresse, G., & Hafner, J. (1994). Ab initiomolecular-dynamics simulation of the liquid-metal–amorphous-semiconductor transition in germanium. Physical Review B, 49(20), 14251–14269.
(56) Pouget, E. M., Bomans, P. H. H., Goos, J. A. C. M., Frederik, P. M., de With, G., & Sommerdijk, N. A. J. M. (2009). The Initial Stages of Template-Controlled CaCO3 Formation Revealed by Cryo-TEM. Science, 323(5920), 1455–1458.
(57) Raiteri, P., & Gale, J. D. (2010). Water Is the Key to Nonclassical Nucleation of Amorphous Calcium Carbonate. Journal of the American Chemical Society, 132(49), 17623–17634.
(58) Wolf, S. E., Leiterer, J., Kappl, M., Emmerling, F., & Tremel, W. (2008). Early Homogenous Amorphous Precursor Stages of Calcium Carbonate and Subsequent Crystal Growth in Levitated Droplets. Journal of the American Chemical Society, 130(37), 12342–12347.
(59) Wallace, A. F., Hedges, L. O., Fernandez-Martinez, A., Raiteri, P., Gale, J. D., Waychunas, G. A., De Yoreo, J. J. (2013). Microscopic Evidence for Liquid-Liquid Separation in Supersaturated CaCO3 Solutions. Science, 341(6148), 885–889.
(60) Smeets, P. J. M., Finney, A. R., Habraken, W. J. E. M., Nudelman, F., Friedrich, H., Laven, J., … Sommerdijk, N. A. J. M. (2017). A classical view on nonclassical nucleation. Proceedings of the National Academy of Sciences, 114(38), E7882–E7890.
(61) Sebastiani, F., Wolf, S. L. P., Born, B., Luong, T. Q., Cölfen, H., Gebauer, D., & Havenith, M. (2016). Water Dynamics from THz Spectroscopy Reveal the Locus of a Liquid-Liquid Binodal Limit in Aqueous CaCO3Solutions. Angewandte Chemie International Edition, 56(2), 490–495.
(62) De Yoreo, J. J., Gilbert, P. U. P. A., Sommerdijk, N. A. J. M., Penn, R. L., Whitelam, S., Joester, D., Dove, P. M. (2015). Crystallization by particle attachment in synthetic, biogenic, and geologic environments. Science, 349(6247), aaa6760–aaa6760.
(63) Faatz, M., Gröhn, F., & Wegner, G. (2004). Amorphous Calcium Carbonate: Synthesis and Potential Intermediate in Biomineralization. Advanced Materials, 16(12), 996–1000.
(64) Rieger, J., Frechen, T., Cox, G., Heckmann, W., Schmidt, C., & Thieme, J. (2007). Precursor structures in the crystallization/precipitation processes of CaCO3 and control of particle formation by polyelectrolytes. Faraday Discussions, 136, 265.

(65) Habraken, W. J. E. M., Tao, J., Brylka, L. J., Friedrich, H., Bertinetti, L., Schenk, A. S., … Sommerdijk, N. A. J. M. (2013). Ion-association complexes unite classical and non-classical theories for the biomimetic nucleation of calcium phosphate. Nature Communications, 4(1).
(66) Epasto, L. M., Georges, T., Selimović, A., Guigner, J.-M., Azaïs, T., & Kurzbach, D. (2021). Formation and Evolution of Nanoscale Calcium Phosphate Precursors under Biomimetic Conditions. Analytical Chemistry, 93(29), 10204–10211.
(67) Lilly Thankamony, A. S., Wittmann, J. J., Kaushik, M., & Corzilius, B. (2017). Dynamic nuclear polarization for sensitivity enhancement in modern solid-state NMR. Progress in Nuclear Magnetic Resonance Spectroscopy, 102-103, 120–195.
(68) Cerreia Vioglio, P., Thureau, P., Juramy, M., Ziarelli, F., Viel, S., Williams, P. A., … Mollica, G. (2019). A Strategy for Probing the Evolution of Crystallization Processes by Low-temperature Solid-state NMR and Dynamic Nuclear Polarization. The Journal of Physical Chemistry Letters.
(69) Juramy, M., Chèvre, R., Cerreia Vioglio, P., Ziarelli, F., Besson, E., Gastaldi, S., … Mollica, G. (2021). Monitoring Crystallization Processes in Confined Porous Materials by Dynamic Nuclear Polarization Solid-State Nuclear Magnetic Resonance. Journal of the American Chemical Society, 143(16), 6095–6103.
(70) Rossini, A. J., Zagdoun, A., Lelli, M., Lesage, A., Copéret, C., & Emsley, L. (2013). Dynamic Nuclear Polarization Surface Enhanced NMR Spectroscopy. Accounts of Chemical Research, 46(9), 1942–1951.
(71) Lesage, A., Lelli, M., Gajan, D., Caporini, M. A., Vitzthum, V., Miéville, P., … Emsley, L. (2010). Surface Enhanced NMR Spectroscopy by Dynamic Nuclear Polarization. Journal of the American Chemical Society, 132(44), 15459–15461.
(72) Pierrick Berruyer; Emsley Lyndon; Anne Lesage. DNP in Materials Science: Touching the Surface. eMagRes. LRM, ISIC-GE January 1, 2018, pp 93–104.
(73) Ajili, W., Laurent, G., Menguy, N., Gansmuller, A. H., Huchette, S., Auzoux-Bordenave, S., … Azais, T. (2020). Chemical Heterogeneities within the Disordered Mineral Domains of Aragonite Platelets in Nacre from the European Abalone Haliotis Tuberculata. The Journal of Physical Chemistry C.
(74) Bewernitz, M. A., Gebauer, D., Long, J., Cölfen, H., & Gower, L. B. (2012). A metastable liquid precursor phase of calcium carbonate and its interactions with polyaspartate. Faraday Discussions, 159, 291.
(75) Dorvee, J. R., & Veis, A. (2013). Water in the formation of biogenic minerals: Peeling away the hydration layers. Journal of Structural Biology, 183(2), 278–303.
(76) Ajili, W., Tovani, C.B., Fouassier, J. et al. (2022). Inorganic phosphate in growing calcium carbonate abalone shell suggests a shared mineral ancestral precursor. Nat Commun 13, 1496 (2022).
(77) Nebel, H., Neumann, M., Mayer, C., & Epple, M. (2008). On the Structure of Amorphous Calcium Carbonate - A Detailed Study by Solid-State NMR Spectroscopy. Inorganic Chemistry, 47(17), 7874–7879.
(78) Schuitemaker, A., Aufort, J., …Gale, J. Simulating the binding of key organic functional groups to aqueous calcium carbonate species. Phys. Chem. Chem. Phys., 2021,23, 27253-27265

(79) Jiang, W., Pacella, M. S., Athanasiadou, D., Nelea, V., Vali, H., Hazen, R. M., … McKee, M. D. (2017). Chiral acidic amino acids induce chiral hierarchical structure in calcium carbonate. Nature Communications, 8, 15066.
(80) Jiang, W., Athanasiadou, D., Zhang, S., Demichelis, R., Koziara, K. B., Raiteri, P., … McKee, M. D. (2019). Homochirality in biomineral suprastructures induced by assembly of single-enantiomer amino acids from a nonracemic mixture. Nature Communications, 10(1).
(81) Ben Shir, I., Kababya, S., Zax, D. B., & Schmidt, A. (2020). Resilient intracrystalline occlusions: a solid-state NMR view of local structure as it tunes bulk lattice properties. Journal of the American Chemical Society.
(82) Tian, J., Yin, Y., Sun, H., & Luo, X. (2002). Magnesium chloride: an efficient 13C NMR relaxation agent for amino acids and some carboxylic acids. Journal of Magnetic Resonance, 159(2), 137–144.
(83) Irving, C. S., Hammer, B. E., Danyluk, S. S., & Klein, P. D. (1980). 13C nuclear magnetic resonance study of the complexation of calcium by taurine. Journal of Inorganic Biochemistry, 13(2), 137–150.
(84) Gebauer, D., Cölfen, H., Verch, A., & Antonietti, M. (2009). The Multiple Roles of Additives in CaCO3Crystallization: A Quantitative Case Study. Advanced Materials, 21(4), 435–439.
(85) Brinker, C. J.; Scherer, G. W. Sol-Gel Science: The Physics and Chemistry of Sol-Gel Processing; Academic Press, 2013
(86) Livage, J.; Henry, M.; Sanchez, C. Sol-Gel Chemistry of Transition Metal Oxides. Progress in Solid State Chemistry 1988, 18 (4), 259–341.
(87) Sanchez, C.; Livage, J.; Henry, M.; Babonneau, F. Chemical Modification of Alkoxide Precursors. Journal of Non-Crystalline Solids 1988, 100 (1–3), 65–76.
(88) Inorganic and Organometallic Polymers with Special Properties; Laine, R. M., Ed.; Springer Netherlands: Dordrecht, 1992
(89) Kallala, M.; Sanchez, C.; Cabane, B. SAXS Study of Gelation and Precipitation in Titanium-Based Systems. Journal of Non-Crystalline Solids 1992, 147–148, 189–193.
(90) Kallala, M.; Sanchez, C.; Cabane, B. Structures of Inorganic Polymers in Sol-Gel Processes Based on Titanium Oxide. Phys. Rev. E 1993, 48 (5), 3692–3704.
(91) Doeuff, S.; Henry, M.; Sanchez, C.; Livage, J. Hydrolysis of Titanium Alkoxides: Modification of the Molecular Precursor by Acetic Acid. Journal of Non-Crystalline Solids 1987, 89 (1–2), 206–216.
(92) Griesmar, P.; Sanchez, C.; Puccetti, G.; Ledoux, I.; Zyss, J. Second-Harmonic Generation from Organic Molecules Incorporated in Sol-Gel Matrices. Mol Eng 1991, 1 (3), 205–220.
(93) Audebert, P.; Griesmar, P.; Sanchez, C. Electrochemical Probing of the Sol–Gel–Xerogel Evolution. J. Mater. Chem. 1991, 1 (4), 699–700.
(94) Bleuzen, A.; Barboux-Doeuff, S.; Flaud, P.; Sanchez, C. Rheological Study of Titanium Oxide-Based Gels. Materials Research Bulletin 1994, 29 (12), 1223–1232.
*(95)* Scolan, E.; Sanchez, C. Synthesis and Characterization of Surface-Protected Nanocrystalline Titania Particles. Chem. Mater. 1998, 1